A HYBRID MODEL FOR THE EVOLUTION OF GALAXIES AND ACTIVE GALACTIC NUCLEI IN THE INFRARED

Zhen-Yi Cai[1,2], Andrea Lapi[1,3], Jun-Qing Xia[1,4], Gianfranco De Zotti[1,5], Mattia Negrello[5], Carlotta Gruppioni[6], Emma Rigby[7], Guillaume Castex[8], Jacques Delabrouille[8], and Luigi Danese[1]

[1] Astrophysics Sector, SISSA, Via Bonomea 265, I-34136 Trieste, Italy; zcai@sissa.it
[2] Department of Astronomy and Institute of Theoretical Physics and Astrophysics, Xiamen University, Xiamen 361005, China
[3] Dipartimento di Fisica, Università "Tor Vergata," Via della Ricerca Scientifica 1, I-00133 Roma, Italy
[4] Key Laboratory of Particle Astrophysics, Institute of High Energy Physics, Chinese Academy of Science, P.O. Box 918-3, Beijing 100049, China
[5] INAF-Osservatorio Astronomico di Padova, Vicolo dell'Osservatorio 5, I-35122 Padova, Italy
[6] INAF-Osservatorio Astronomico di Bologna, via Ranzani 1, I-40127 Bologna, Italy
[7] Leiden Observatory, P.O. Box 9513, 2300-RA Leiden, The Netherlands
[8] APC, 10, rue Alice Domon et Léonie Duquet, F-75205 Paris Cedex 13, France

ABSTRACT

We present a comprehensive investigation of the cosmological evolution of the luminosity function of galaxies and active galactic nuclei (AGNs) in the infrared (IR). Based on the observed dichotomy in the ages of stellar populations of early-type galaxies on one side and late-type galaxies on the other, the model interprets the epoch-dependent luminosity functions at $z \geqslant 1.5$ using a physical approach for the evolution of proto-spheroidal galaxies and of the associated AGNs, while IR galaxies at $z < 1.5$ are interpreted as being mostly late-type "cold" (normal) and "warm" (starburst) galaxies. As for proto-spheroids, in addition to the epoch-dependent luminosity functions of stellar and AGN components separately, we have worked out, for the first time, the evolving luminosity functions of these objects as a whole (stellar plus AGN component), taking into account in a self-consistent way the variation with galactic age of the global spectral energy distribution. The model provides a physical explanation for the observed positive evolution of both galaxies and AGNs up to $z \simeq 2.5$ and for the negative evolution at higher redshifts, for the sharp transition from Euclidean to extremely steep counts at (sub-)millimeter wavelengths, as well as the (sub-)millimeter counts of strongly lensed galaxies that are hard to account for by alternative, physical or phenomenological, approaches. The evolution of late-type galaxies and $z < 1.5$ AGNs is described using a parametric phenomenological approach. The modeled AGN contributions to the counts and to the cosmic infrared background (CIB) are always sub-dominant. They are maximal at mid-IR wavelengths: the contribution to the 15 and 24 μm counts reaches 20% above 10 and 2 mJy, respectively, while the contributions to the CIB are of 8.6% and of 8.1% at 15 μm and 24 μm, respectively. The model provides a good fit to the multi-wavelength (from the mid-IR to millimeter waves) data on luminosity functions at different redshifts and on number counts (both global and per redshift slices). A prediction of the present model, useful to test it, is a systematic variation with wavelength of the populations dominating the counts and the contributions to the CIB intensity. This implies a specific trend for cross-wavelength CIB power spectra, which is found to be in good agreement with the data.

Key words: galaxies: elliptical and lenticular, cD – galaxies: evolution – galaxies: formation – galaxies: high-redshift – submillimeter: galaxies

Online-only material: color figures

1. INTRODUCTION

The huge amount of infrared (IR) to millimeter-wave data that has been accumulating over the last several years has not yet led to a fully coherent, established picture of the cosmic star formation history, of the IR evolution of active galactic nuclei (AGNs), and of the interrelations between star formation and nuclear activity.

Many increasingly sophisticated phenomenological models for the cosmological evolution of the galaxy and AGN luminosity functions (LFs) over a broad wavelength range have been worked out (e.g., Béthermin et al. 2012a, 2011; Gruppioni et al. 2011; Rahmati & van der Werf 2011; Marsden et al. 2011; Franceschini et al. 2010; Valiante et al. 2009; Le Borgne et al. 2009; Rowan-Robinson 2009). These models generally include multiple galaxy populations, with different spectral energy distributions (SEDs) and different evolutionary properties, described by simple analytic formu-

lae. In some cases AGNs are also taken into account. All of them, however, admittedly have limitations.

The complex combination of source properties (both in terms of the mixture of SEDs and of evolutionary properties), called for by the richness of data, results in a large number of parameters, implying substantial degeneracies that hamper the interpretation of the results. The lack of constraints coming from the understanding of the astrophysical processes controlling the evolution and the SEDs limits the predictive capabilities of these models. In fact, predictions of pre-*Herschel* phenomenological models, matching the data then available, yielded predictions for *Herschel* counts quite discrepant from each other and with the data.

The final goal is a physical model linking the galaxy and AGN formation and evolution to primordial density perturbations. In this paper we make a step in this direction presenting a comprehensive "hybrid" approach, combining a physical, forward model for spheroidal galaxies and the early evolution

of the associated AGNs with a phenomenological backward model for late-type galaxies and for the later AGN evolution. We start from the consideration of the observed dichotomy in the ages of stellar populations of early-type galaxies on one side and late-type galaxies on the other. Early-type galaxies and massive bulges of Sa galaxies are composed of relatively old stellar populations with mass-weighted ages of $\gtrsim$8–9 Gyr (corresponding to formation redshifts $z \gtrsim 1$–1.5), while the disk components of spiral and irregular galaxies are characterized by significantly younger stellar populations. For instance, the luminosity-weighted age for most of Sb or later-type spirals is $\lesssim$7 Gyr (cf. Bernardi et al. 2010, their Figure 10), corresponding to a formation redshift $z \lesssim 1$. Thus proto-spheroidal galaxies are the dominant star-forming population at $z \geqslant 1.5$, while IR galaxies at $z < 1.5$ are mostly late-type "cold" (normal) and "warm" (starburst) galaxies.

Fuller hierarchical galaxy formation models, whereby the mass assembly of galaxies is related to structure formation in the dark matter and the star formation and merger histories of galaxies of all morphological types are calculated based on physical prescriptions have been recently presented by several groups (Lacey et al. 2008; Fontanot et al. 2009; Narayanan et al. 2010; Shimizu et al. 2012). However, the predictions for the IR evolution of galaxies are limited to a small set of wavelengths and frequently highlight serious difficulties with accounting for observational data (Lacey et al. 2010; Niemi et al. 2012; Hayward et al. 2013).

While the evolution of dark matter halos in the framework of the "concordance" ΛCDM cosmology is reasonably well understood thanks to N-body simulations such as the Millennium, the Millennium-XXL, and the Bolshoi simulations (Springel et al. 2005; Boylan-Kolchin et al. 2009; Angulo et al. 2012; Klypin et al. 2011), establishing a clear connection between dark matter halos and visible objects proved to be quite challenging, especially at (sub-)millimeter wavelengths. The early predictions of the currently favored scenario, whereby both the star formation and the nuclear activity are driven by mergers, were more than one order of magnitude below the observed SCUBA 850 μm counts (Kaviani et al. 2003; Baugh et al. 2005). The basic problem is that the duration of the star formation activity triggered by mergers is too short, requiring non-standard assumptions either on the initial mass function (IMF) or on dust properties to account for the measured source counts. The problem is more clearly illustrated in terms of redshift-dependent far-IR/submillimeter LF, estimated on the basis of *Herschel* data (Eales et al. 2010; Gruppioni et al. 2010; Lapi et al. 2011). These estimates consistently show that $z \simeq 2$ galaxies with star formation rates (SFRs) SFR $\simeq 300\,M_\odot$ yr^{-1} have comoving densities $\Phi_{300} \sim 10^{-4}$ Mpc^{-3} dex^{-1}. The comoving density of the corresponding halos is $n(M_{\rm vir}) \sim \Phi_{300}(t_{\rm exp}/\tau_{\rm SFR})$, where $M_{\rm vir}$ is the total virial mass (mostly dark matter), $\tau_{\rm SFR}$ is the lifetime of the star-forming phase, and $t_{\rm exp}$ is the expansion timescale. For the fiducial lifetime $\tau_{\rm SFR} \simeq 0.7$ Gyr advocated by Lapi et al. (2011), $\log(M_{\rm vir}/M_\odot) \simeq 12.92$, while for $\tau_{\rm SFR} \simeq 0.1$ Gyr, typical of a merger-driven starburst, $\log(M_{\rm vir}/M_\odot) \simeq 12.12$. Thus while the Lapi et al. (2011) model implies an SFR/$M_{\rm vir}$ ratio easily accounted for on the basis of standard IMFs and dust properties, the latter scenario requires an SFR/$M_{\rm vir}$ ratio more than a factor of six higher.

To reach the required values of SFR/$M_{\rm vir}$ or, equivalently, of $L_{\rm IR}/M_{\rm vir}$, Baugh et al. (2005) resorted to a top-heavy IMF while Kaviani et al. (2003) assumed that the bulk of the submillimeter emission comes from a huge amount of cool dust.

But even tweaking with the IMF and with dust properties, fits of the submillimeter counts obtained within the merger-driven scenario (Lacey et al. 2010; Niemi et al. 2012) are generally unsatisfactory. Further constraints on physical models come from the clustering properties of submillimeter galaxies that are determined by their effective halo masses. As shown by Xia et al. (2012), both the angular correlation function of detected submillimeter galaxies and the power spectrum of fluctuations of the cosmic infrared background (CIB) indicate halo masses larger than implied by the major mergers plus top-heavy initial stellar mass function scenario (Kim et al. 2012) and smaller than implied by cold flow models but consistent with the self-regulated baryon collapse scenario (Granato et al. 2004; Lapi et al. 2006, 2011).

As is well known, the strongly negative K-correction emphasizes high-z sources at (sub-)millimeter wavelengths. The data show that the steeply rising portion of the (sub-)millimeter counts is indeed dominated by ultra-luminous star-forming galaxies with a redshift distribution peaking at $z \simeq 2.5$ (Chapman et al. 2005; Aretxaga et al. 2007; Yun et al. 2012; Smolčić et al. 2012). As shown by Lapi et al. (2011), the self-regulated baryon collapse scenario provides a good fit of the (sub-)millimeter data (counts, redshift-dependent LFs) as well as of the stellar mass functions at different redshifts. Moreover, the counts of strongly lensed galaxies were predicted with remarkable accuracy (Negrello et al. 2007, 2010; Lapi et al. 2012; González-Nuevo et al. 2012). Further considering that this scenario accounts for the clustering properties of submillimeter galaxies (Xia et al. 2012), we conclude that it is well grounded, and we adopt it for the present analysis. However, we upgrade this model in two respects. First, while on one side, the model envisages a co-evolution of spheroidal galaxies and active nuclei at their centers, the emissions of the two components have so far been treated independently of each other. This is not a problem in the wavelength ranges where one of the two components dominates, as in the (sub-)millimeter region where the emission is dominated by star formation, but is no longer adequate at mid-IR wavelengths, where the AGN contribution may be substantial. In this paper, we present and exploit a consistent treatment of proto-spheroidal galaxies including both components. Second, while the steeply rising portion of (sub-)millimeter counts is fully accounted for by proto-spheroidal galaxies, late-type (normal and starburst) galaxies dominate both at brighter and fainter flux densities and over broad flux density ranges at mid-IR wavelengths. At these wavelengths, AGNs not associated with proto-spheroidal galaxies but either to evolved early-type galaxies or to late-type galaxies are also important. Since we do not have a physical evolutionary model for late-type galaxies and the associated AGNs, these source populations have been dealt with adopting a phenomenological approach.

Another distinctive feature of the present model is that we have attempted to simultaneously fit the data over a broad wavelength range, from mid-IR to millimeter waves. As mentioned in several papers, this presents several challenges. First, the data come from different instruments and the relative calibration is sometimes problematic (see the discussion in Béthermin et al. 2011). Systematic calibration offsets may hinder simultaneous fits of different data sets. For example, Marsden et al. (2011) pointed out that there is considerable tension between the SCUBA 850 μm counts and the AzTEC counts at 1.1 mm, and indeed the 850 μm and millimeter-wave counts have been repeatedly corrected (generally downward) as biases were discovered and better data were acquired. Also, the very complex

SEDs in the mid-IR, where strong polycyclic aromatic hydrocarbon (PAH) emission features show up, make the counts exceedingly sensitive to the details of the spectral response function of the specific instrument and introduce large uncertainties in the conversion from broadband measurements to monochromatic flux densities giving rise to strong discrepancies among data sets nominally referring to the same wavelength. In fact, large discrepancies are present among different determinations of $15\,\mu$m and $60\,\mu$m source counts.

The plan of the work is as follows. In Section 2, we describe the physical model for the evolution of proto-spheroidal galaxies and of the associated AGNs and the SEDs adopted for these sources. Section 3 deals with the evolutionary model for late-type galaxies and $z \leqslant 1.5$ AGNs. In Section 4, we present the formalism to compute the source counts of unlensed and lensed sources, the cumulative flux density as a function of redshift, and the contributions to the CIB. In Section 5, we report on the determination of the best-fit values of the model parameters. In Section 6, the model results are compared with data on multi-frequency LFs at various redshifts and on source counts, both total and per redshift slices. The multi-frequency power spectra of CIB fluctuations implied by the model are discussed in Section 7. Finally, Section 8 contains a summary of the paper and our main conclusions.

Tabulations of multi-frequency model counts, redshift distributions, SEDs, redshift-dependent LFs at several wavelengths, and a large set of figures comparing model predictions with the data are available at the Web site http://people.sissa.it/~zcai/galaxy_agn/.

Throughout this paper we adopt a flat cosmology with present-day matter and baryon density in units of the critical density, $\Omega_{m,0} = 0.27$ and $\Omega_{b,0} = 0.044$; Hubble constant $h = H_0/100 = 0.71$; spectrum of primordial density perturbations with slope $n = 1$ and normalization on a scale of $8\,h^{-1}$ Mpc $\sigma_8 = 0.81$.

2. STAR-FORMING PROTO-SPHEROIDAL GALAXIES

2.1. Overview of the Model

We adopt the model by Granato et al. (2004; see also Lapi et al. 2006, 2011; Mao et al. 2007) that interprets powerful high-z submillimeter galaxies as massive proto-spheroidal galaxies in the process of forming most of their stellar mass. It hinges upon high-resolution numerical simulations showing that dark matter halos form in two stages (Zhao et al. 2003; Wang et al. 2011; Lapi & Cavaliere 2011). An early fast collapse of the halo bulk, including a few major merger events, reshuffles the gravitational potential and causes the dark matter and stellar components to undergo (incomplete) dynamical relaxation. A slow growth of the halo outskirts in the form of many minor mergers and diffuse accretion follows; this second stage has little effect on the inner potential well where the visible galaxy resides.

The star formation is triggered by the fast collapse/merger phase of the halo and is controlled by self-regulated baryonic processes. It is driven by the rapid cooling of the gas within a region with radius $\approx 30\%$ of the halo virial radius, i.e., of $\simeq 70(M_{\rm vir}/10^{13}\,M_\odot)^{1/3}[(1 + z_{\rm vir})/3]^{-1}$ kpc, where $M_{\rm vir}$ is the halo mass and $z_{\rm vir}$ is the virialization redshift, encompassing about 40% of the total mass (dark matter plus baryons). The star formation and the growth of the central black hole, which are regulated by the energy feedback from supernovae (SNe) and from the active nucleus, are very soon obscured by dust and are

quenched by quasar feedback. The AGN feedback is relevant especially in the most massive galaxies and is responsible for their shorter duration (5–7×10^8 yr) of the active star-forming phase. In less massive proto-spheroidal galaxies, the SFR is mostly regulated by SN feedback and continues for a few Gyr. Only a minor fraction of the gas initially associated with the dark matter halo is converted into stars. The rest is ejected by feedback processes.

The equations governing the evolution of the baryonic matter in dark matter halos and the adopted values for the parameters are given in the Appendix where some examples of the evolution with galactic age (from the virialization time) of quantities related to the stellar and to the AGN component are also shown. For additional details and estimates of physically plausible ranges for each parameter we refer to Granato et al. (2004), Lapi et al. (2006), and Mao et al. (2007). Since spheroidal galaxies are observed to be in passive evolution at $z \lesssim 1$–1.5 (e.g., Renzini 2006), they are bright at submillimeter wavelengths only at higher redshifts.

2.2. Luminosity Functions

The bolometric LF of proto-spheroids is obtained convolving the halo formation rate $dN_{\rm ST}(M_{\rm vir}, z)/dt$ with the galaxy luminosity distribution, $P(L, z; M_{\rm vir})$. The halo formation rate is well approximated, for $z \gtrsim 1.5$, by the positive term of the cosmic time derivative of the halo mass function $N_{\rm ST}$. For the latter, giving the average comoving number density of halos of given mass, $M_{\rm vir}$, we adopt the Sheth & Tormen (1999) analytical expression

$$N_{\rm ST}(M_{\rm vir}, z)dM_{\rm vir} = \frac{\bar{\rho}_{m,0}}{M_{\rm vir}^2} f_{\rm ST}(\nu) \frac{d\ln\nu}{d\ln M_{\rm vir}} dM_{\rm vir}, \quad (1)$$

where $\bar{\rho}_{m,0} = \Omega_{m,0}\rho_{c,0}$ is the present-day mean comoving matter density of the universe and $\nu \equiv [\delta_c(z)/\sigma(M_{\rm vir})]^2$, with $\delta_c(z) = \delta_0(z)D(0)/D(z)$. The critical value of the initial overdensity that is required for spherical collapse at z, $\delta_0(z)$, is (Nakamura & Suto 1997)

$$\delta_0(z) = \frac{3(12\pi)^{2/3}}{20}[1 + 0.0123\log\Omega_m(z)]$$
$$\simeq 1.6865[1 + 0.0123\log\Omega_m(z)].$$

The linear growth factor can be approximated as (Lahav et al. 1991; Carroll et al. 1992)

$$D(z) = \frac{5\Omega_m(z)}{2(1 + z)} \bigg/ \left[\frac{1}{70} + \frac{209}{140}\Omega_m(z) - \frac{1}{140}\Omega_m^2(z) + \Omega_m^{4/7}(z)\right].$$

The mass variance $\sigma(M_{\rm vir})$ of the primordial perturbation field smoothed on a scale containing a mass $M_{\rm vir}$ with a top-hat window function was computed using the Bardeen et al. (1986) power spectrum with correction for baryons (Sugiyama 1995), for our choice of cosmological parameters (see Section 1). The results are accurately approximated (error $< 1\%$ over a broad range of $M_{\rm vir}$, $10^6 < M_{\rm vir}/M_\odot < 10^{16}$) by

$$\sigma(M_{\rm vir}) = \frac{0.8}{0.84}[14.110393 - 1.1605397x - 0.0022104939x^2$$
$$+ 0.0013317476x^3 - 2.1049631 \times 10^{-6}x^4] \quad (2)$$

where $x \equiv \log(M_{\rm vir}/M_\odot)$. Furthermore

$$f_{\rm ST}(\nu) = A[1 + (a\nu)^{-p}]\left(\frac{a\nu}{2}\right)^{1/2}\frac{e^{-a\nu/2}}{\pi^{1/2}},$$

where $A = 0.322$, $p = 0.3$, and $a = 0.707$.
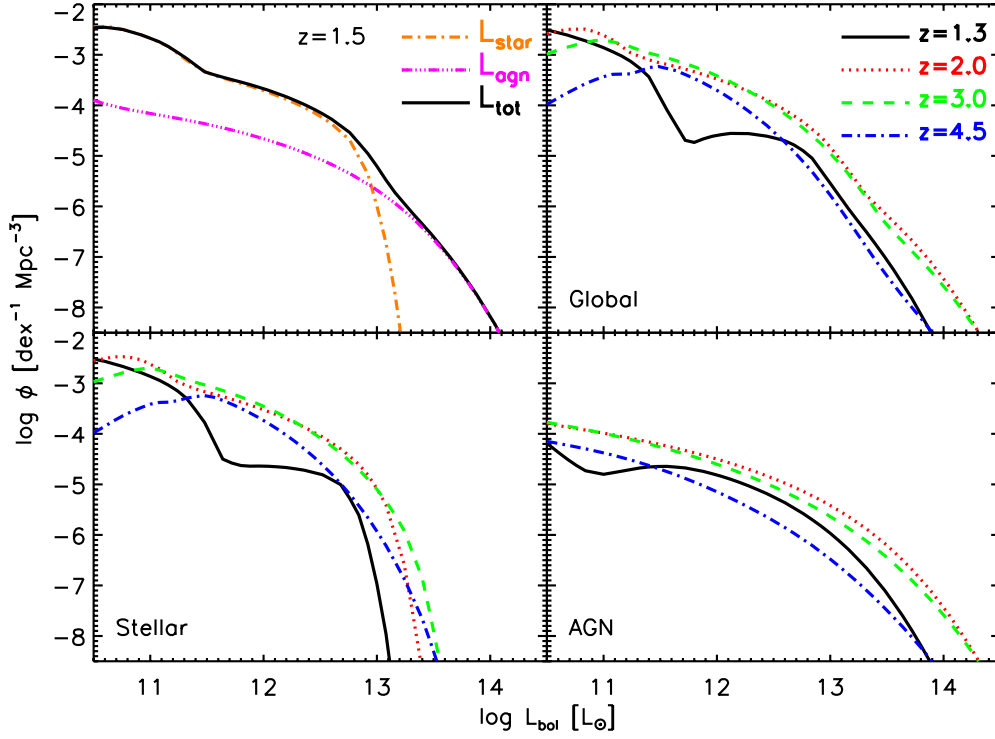
Figure 1. Bolometric luminosity functions of proto-spheroidal galaxies. The upper left panel shows the luminosity functions at $z = 1.5$ of the stellar (dot-dashed orange line) and of the AGN component luminosity (triple-dot-dashed magenta line), as well as the global luminosity function (solid black line). Note that, as discussed in Section 2.2, the latter is *not* the sum of the two components although in this case is very close to it. The upper right panel illustrates the evolution of the global luminosity function from $z = 1.3$ to $z = 4.5$, while the lower panels show the evolution of each component separately. The decline at low luminosities is an artifact due to the adopted lower limit to the proto-spheroid halo masses. The figure highlights the different shapes of the stellar and AGN bolometric luminosity function, with the latter having a more extended high luminosity tail, while the former sinks down exponentially above $\sim 10^{13}$ $L_\odot$. The evolutionary behavior of the two components is qualitatively similar and cannot be described as simple luminosity or density evolution; down-sizing effects are visible in both cases. On the other hand there are also clear differences.

(A color version of this figure is available in the online journal.)

The halo formation rate is then

$$\frac{dN_{ST}(M_{vir}, z)}{dt} = N_{ST}(M_{vir}, z)\frac{d\ln f_{ST}(\nu)}{dt}$$

$$= -N_{ST}(M_{vir}, z)\left[\frac{a\delta_c}{\sigma^2} + \frac{2p}{\delta_c}\frac{\sigma^{2p}}{\sigma^{2p} + a^p\delta_c^{2p}} - \frac{1}{\delta_c}\right]\frac{d\delta_c}{dz}\frac{dz}{dt}$$

$$\simeq N_{ST}(M_{vir}, z)\left[\frac{a\nu}{2} + \frac{p}{1 + (a\nu)^p}\right]\frac{d\ln\nu}{dz}\left|\frac{dz}{dt}\right|, \quad (3)$$

where $dz/dt = -H_0(1 + z)E(z)$ with $E(z) \equiv \sqrt{\Omega_{\Lambda,0} + \Omega_{m,0}(1 + z)^3}$.

The comoving differential LF $\Phi(\log L, z)$, i.e., the number density of galaxies per unit $\log L$ interval at redshift z, is given by

$$\Phi(\log L, z) = \int_{M_{vir}^{min}}^{M_{vir}^{max}} dM_{vir} \int_z^{z_{vir}^{max}} dz_{vir} \left|\frac{dt_{vir}}{dz_{vir}}\right| \frac{dN_{ST}}{dt_{vir}}(M_{vir}, z_{vir})$$
$$\cdot P(\log L, z; M_{vir}, z_{vir}), \quad (4)$$

where $P(\log L, z; M_{vir}, z_{vir})$ is the luminosity distribution of galaxies at redshift z inside a halo of mass M_{vir} virialized at redshift z_{vir}. We set $z_{vir}^{min} = 1.5$ and $z_{vir}^{max} = 12$.

As mentioned in Section 2.1, the total luminosity of a galaxy is the sum of those of the stellar component and of the active nucleus. For each component, we assume a log-normal

luminosity distribution

$$P[\log L | \log \bar{L}]d\log L = \frac{\exp[-\log^2(L/\bar{L})/2\sigma^2]}{\sqrt{2\pi\sigma^2}}d\log L, \quad (5)$$

with dispersion $\sigma_* = 0.10$ around the mean stellar luminosity $\bar{L}_*(z; M_{vir}, z_{vir})$ and $\sigma_\bullet = 0.35$ around the mean AGN luminosity $\bar{L}_\bullet(z; M_{vir}, z_{vir})$. The mean luminosities are computed solving the equations detailed in the Appendix. The higher luminosity dispersion for the AGN component reflects its less direct relationship, compared to the stellar component, with M_{vir} and z_{vir}. The distribution of the total luminosity, $L_{tot} = L_* + L_\bullet$, is then (Dufresne 2004)

$$P[\log L_{tot} | \log \bar{L}_*, \log \bar{L}_\bullet]d\log L_{tot} = d\log L_{tot}$$
$$\times \int_{-\infty}^{\log L_{tot}} \frac{dx}{2\pi\sigma_*\sigma_\bullet} \frac{L_{tot}}{L_{tot} - 10^x} \exp\{-(x - \log\bar{L}_*)^2/2\sigma_*^2\}$$
$$\times \exp\{-[\log(L_{tot} - 10^x) - \log\bar{L}_\bullet]^2/2\sigma_\bullet^2\}. \quad (6)$$

In the upper left panel of Figure 1 we show, as an example, the bolometric LFs at $z = 1.5$ of the stellar and of the AGN components, as well as the LF of the objects as a whole. As shown in Equation (6), the latter is different from the sum of the first two, although in this case the difference is difficult to perceive. The bright end is dominated by QSOs shining unobstructed after having swept away the interstellar medium
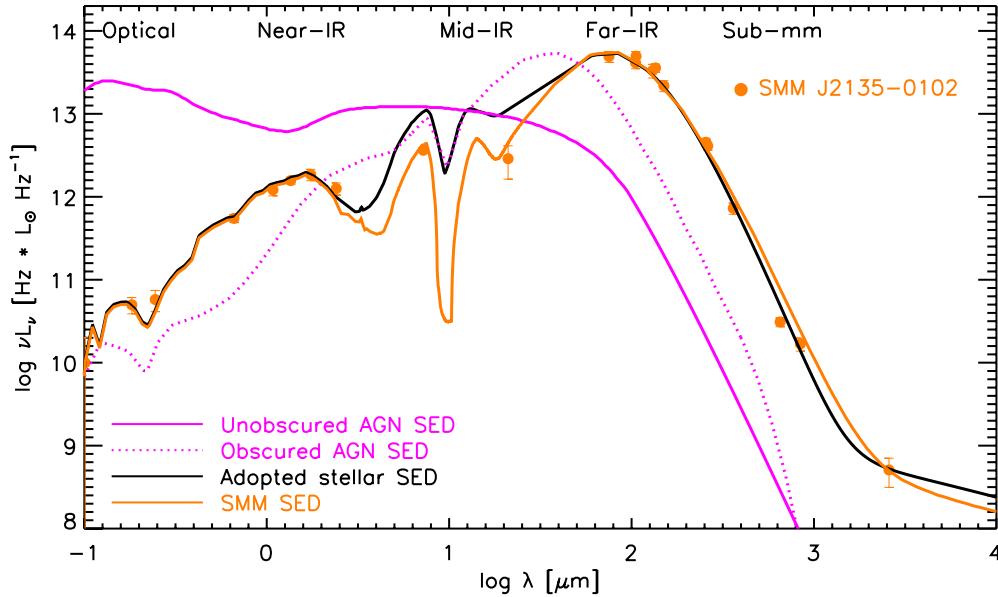
Figure 2. SEDs of stellar and AGN components of proto-spheroidal galaxies. The solid black line shows the adopted SED for the stellar component, obtained modifying that of the $z \simeq 2.3$ galaxy SMM J2135-0102, also shown for comparison (solid orange line; the photometric data are from Swinbank et al. 2010 and Ivison et al. 2010). The dotted magenta line represents the SED adopted for the dust obscured phase of the AGN evolution and is taken from the AGN SED library by Granato & Danese (1994). For unobscured AGNs, we have adopted the mean QSO SED of Richards et al. (2006; solid magenta line). The original SMM J2135-0102 SED and the two AGN SEDs are normalized to $\log(L_{IR}/L_{\odot}) = 13.85$, while the modified SED is normalized to $\log(L_{IR}/L_{\odot}) = 13.92$ to facilitate the comparison with the original SED. Except in the rare cases in which the AGN bolometric luminosity is much larger than that of the starburst, the AGN contribution is small at (sub-)millimeter wavelengths, while it is important and may be dominant in the mid-IR.

(A color version of this figure is available in the online journal.)

(ISM) of the host galaxy. In this phase the QSOs reach their maximum luminosity. Around $\log(L_{bol}/L_{\odot}) \simeq 13$ the AGNs and the starbursts give similar contributions to the bolometric LF. The inflection at $\log(L_{IR}/L_{\odot}) \simeq 11.7$ corresponds to the transition from the regime where the feedback is dominated by SNe (lower halo masses) to the regime where it is dominated by AGNs. While the star formation in massive halos is abruptly stopped by the AGN feedback after 0.5–0.7 Gyr, it lasts much longer in smaller galaxies, implying a fast increase of their number density.

The upper right panel of the same figure illustrates the evolution with cosmic time of the global LF. The cooling and free-fall timescales shorten with increasing redshift because of the increase of the matter density and this drives a positive luminosity evolution, thwarted by the decrease in the comoving density of massive halos. The two competing factors result, for both the starburst and the AGN component (see the lower panels of the figure), in a positive evolution up to $z \simeq 2.5$ followed by a decline at higher z, consistent with the observational determinations by Gruppioni et al. (2010) and Lapi et al. (2011) for the starburst component and by Assef et al. (2011) and Brown et al. (2006) for AGNs. The decrease of the LF at low luminosities, more clearly visible at the higher redshifts, is an artifact due to the adopted lower limit for the considered halo masses. This part of the LF, however, does not contribute significantly to the observed statistics and therefore is essentially irrelevant here. Below the minimum virialization redshift, $z_{vir}^{min} = 1.5$, the bolometric LF of proto-spheroidal galaxies rapidly declines as they evolve toward the "passive" phase. The decline is faster at the bright end (above $\log(L_{bol}/L_{\odot}) \simeq 12$) since the switching off of the star formation for the more massive halos occurs on a shorter timescale.

The monochromatic LFs of each component or of objects as a whole can obviously be computed using the same for-malism, given the respective SEDs. We define $\bar{\mathcal{L}}_{*,\nu} \equiv \nu\bar{L}_{*,\nu} = \nu f_*(\nu)\bar{L}_{*,IR}$, $\bar{\mathcal{L}}_{\bullet,\nu} \equiv \nu\bar{L}_{\bullet,\nu} = \nu f_\bullet(\nu)\bar{L}_{\bullet,bol}$, and $\bar{\mathcal{L}}_\nu \equiv \bar{\mathcal{L}}_{*,\nu} + \bar{\mathcal{L}}_{\bullet,\nu}$, where $f(\nu)$ is the normalized SED ($\int d\nu\, f(\nu) = 1$).

Since the model cannot follow in detail the evolution of the AGN SEDs during the short phase when they shine unobstructed by the ISM of the host galaxy, the distinction between obscured and unobscured AGNs in the model is made in two ways. First, following Lapi et al. (2006), we choose a fixed optical (B-band) "visibility time," $\Delta t_{vis} = 5 \times 10^7$ yr, consistent with current estimates of the optically bright QSO phase. Alternatively, we set the beginning of the optical bright phase at the moment when the gas mass fraction is low enough to yield a low optical depth. We estimate that this corresponds to a gas fraction within the dark matter potential well $f_{gas} = M_{gas}/M_{vir} \lesssim f_{gas,crit} = 0.03$. The two approaches give very similar results and we have chosen the criterion $f_{gas} \lesssim f_{gas,crit}$ to compute the LFs at optical wavelengths.

2.3. Spectral Energy Distributions

Although there is evidence that the galaxy SEDs vary with luminosity (e.g., Smith et al. 2012), Lapi et al. (2011) have shown that the submillimeter data can be accurately reproduced using a single SED for proto-spheroidal galaxies, i.e., the SED of the strongly lensed $z \simeq 2.3$ galaxy SMM J2135-0102 (Swinbank et al. 2010; Ivison et al. 2010), modeled using GRASIL (Silva et al. 1998). The basic reason for the higher uniformity of the SEDs of high-z active star-forming galaxies compared to galaxies at low-z is that the far-IR emission of the former objects comes almost entirely from dust in molecular clouds, heated by newly formed stars, while in low-z galaxies there are important additional contributions from colder "cirrus" heated by older stellar populations.
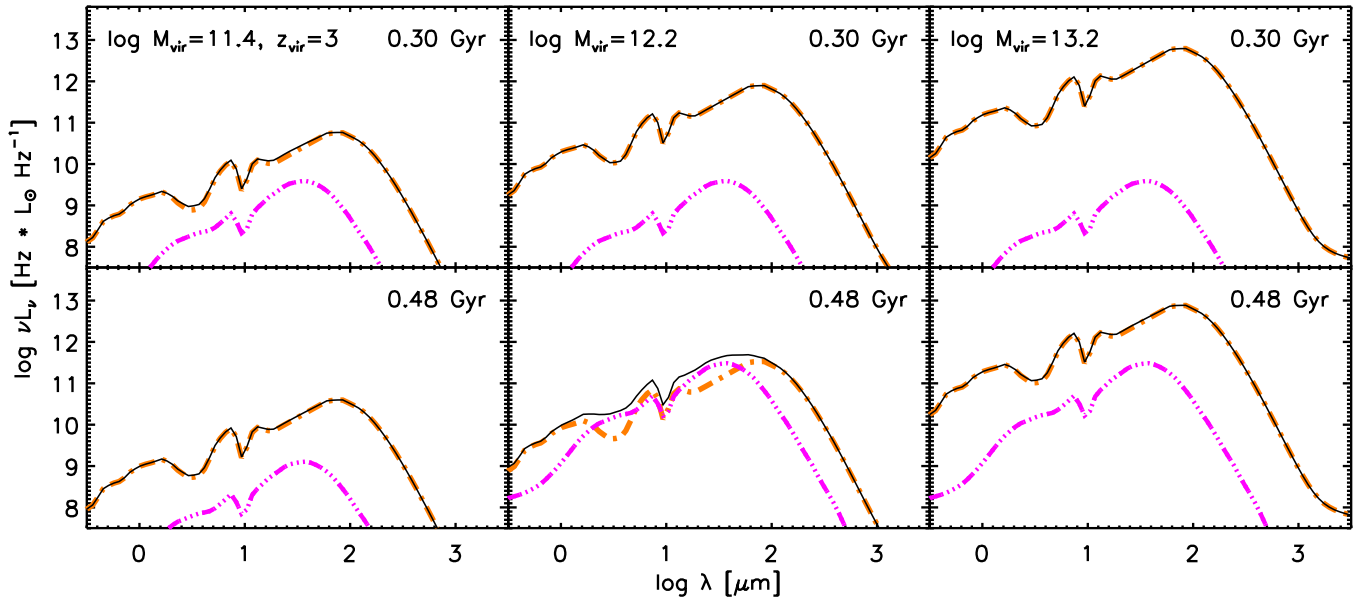
Figure 3. Global SEDs (solid black lines) for two galactic ages (0.3 and 0.48 Gyr) and three host halo masses ($\log(M_H/M_\odot) = 11.4$, 12.2, and 13.2, from left to right), virialized at $z_{\rm vir} = 3$. The dot-dashed orange line (overlaid by the solid black line in some panels) and the triple-dot-dashed magenta line show the stellar and the AGN component, respectively. The shorter evolution timescale of the AGNs is clearly visible. The effect of feedback as a function of halo mass on the SFR is very different from that on accretion onto the supermassive black hole (see the text).

(A color version of this figure is available in the online journal.)

This SED worked very well at submillimeter wavelengths but yielded millimeter-wave counts in excess of the observed ones. To overcome this problem the submillimeter slope of the SED has been made somewhat steeper, preserving the consistency with the photometric data on SMM J2135-0102 (see Figure 2). Moreover, the SED used by Lapi et al. has a ratio between the total (8–1000 μm) IR and the 8 μm luminosity (IR8 = $L_{\rm IR}/L_8$) of $\simeq 30$, far higher than the mean value for $z \simeq 2$ galaxies (IR8 $\simeq 9$; Reddy et al. 2012). We have therefore modified the near- and mid-IR portions of the SED adopting a shape similar to that of Arp 220. The contribution of the passive evolution phase of early-type galaxies is small in the frequency range of interest here and will be neglected.

As mentioned in Section 2.1, the model follows the AGN evolution through two phases (a third phase, reactivation, will be considered in Section 3.2). For the first phase, when the black hole growth is enshrouded by the abundant, dusty ISM of the host galaxy, we adopt the SED of a heavily absorbed AGN taken from the AGN SED library by Granato & Danese (1994). Note that these objects differ from the classical type 2 AGNs because they are not obscured by a circumnuclear torus but by the more widely distributed dust in the host galaxy. They will be referred to as type 3 AGNs. In the second phase the AGN shines after having swept out the galaxy ISM. For this phase, we adopted the mean QSO SED by Richards et al. (2006) extended to submillimeter wavelengths assuming a graybody emission with dust temperature $T_{\rm dust} = 80$ K and emissivity index $\beta = 1.8$. These SEDs imply that the IR (8–1000 μm) band comprises 92% of the bolometric luminosity of obscured AGNs and 19% of that of the unobscured ones. As illustrated by Figure 2, except in the rare cases in which the AGN bolometric luminosity is much larger than that of the starburst, the AGN contribution is small at (sub-)millimeter wavelengths, while it is important and may be dominant in the mid-IR. This implies that the statistics discussed here are insensitive to the parameters describing the extrapolation of the Richards et al. SED to (sub-)millimeter wavelengths.

Figure 3 shows the global SEDs and the contributions of the stellar and AGN components for two galaxy ages and three host halo masses virialized at $z_{\rm vir} = 3$. The shorter evolution timescale of the AGNs is clearly visible. It is worth noting that the effect of feedback as a function of halo mass on the SFR is very different from that on accretion onto the supermassive black hole. In the less massive halos the AGN feedback has only a moderate effect on the evolution of the SFR and of the accretion rate, which are mostly controlled by the SN feedback. With reference to the figure, for $\log(M_{\rm vir}/M_\odot) = 11.4$, the star formation continues at an almost constant rate for a few Gyr. On the other hand, the accretion rate onto the central black hole is at the Eddington limit only up to an age of $\simeq 0.3$ Gyr and afterward drops to a strongly sub-Eddington regime. This is because the growth rate of the reservoir is approximately proportional to the SFR (and therefore slowly varying for few Gyr), while the accretion rate grows exponentially until the mass contained in the reservoir is exhausted. From this moment on the accretion rate is essentially equal to the (strongly sub-Eddington) inflow rate. For more massive halos the quenching of both the SFR and of the accretion occurs more or less simultaneously at ages of $\simeq 0.5$–0.6 Gyr, but while the SFR stops very rapidly, the AGN activity continues until the flow of the matter accumulated in the reservoir runs out. At ages $\gtrsim 0.6$ Gyr, the more massive galaxies are in passive evolution and therefore very weak in the far-IR, while star formation and the dust emission are still present in lower-mass galaxies.

3. LOW-REDSHIFT ($z \lesssim 1.5$) POPULATIONS

3.1. Late-type and Starburst Galaxies

We consider two $z \lesssim 1.5$ galaxy populations: "warm" starburst galaxies and "cold" (normal) late-type galaxies. For the IR LF of both populations, we adopt the functional form
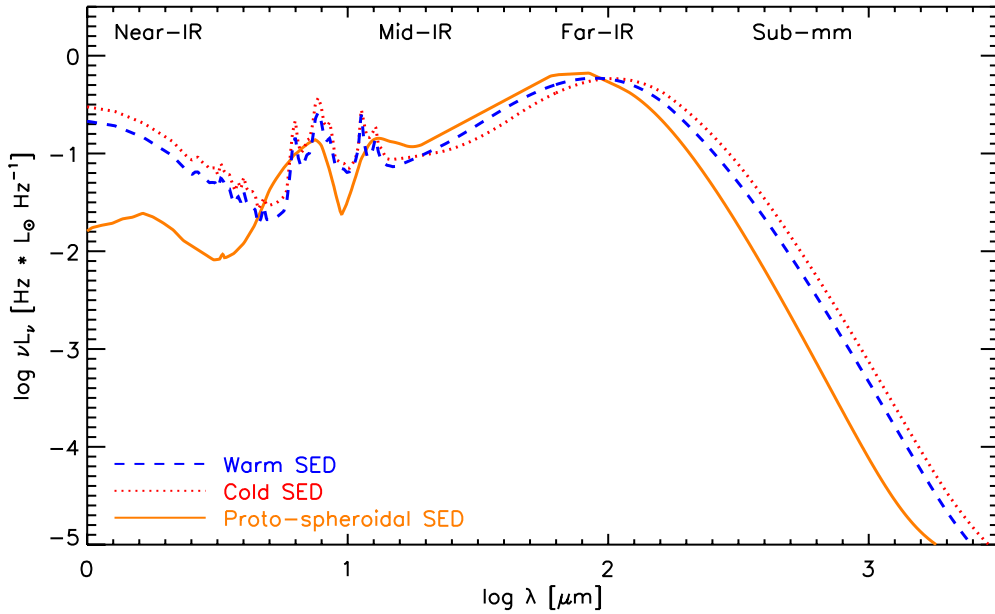
Figure 4. Adopted SEDs for the "warm" (dashed blue line) and "cold" (dotted red line) low-z star-forming galaxies. They were generated combining SEDs of Dale & Helou (2002) and Smith et al. (2012), as described in the text. The solid orange line shows, for comparison, the SED of proto-spheroidal galaxies. The three SEDs are normalized to the same total IR luminosity $\log(L_{IR}/L_\odot) = 1$.
(A color version of this figure is available in the online journal.)

advocated by Saunders et al. (1990):

$$\Phi(\log L_{IR}, z)d \log L_{IR} = \Phi^* \left(\frac{L_{IR}}{L^*} \right)^{1-\alpha}$$

$$\times \exp \left[-\frac{\log^2(1 + L_{IR}/L^*)}{2\sigma^2} \right] d \log L_{IR}, \qquad (7)$$

where the characteristic density Φ^* and luminosity L^*, the low-luminosity slope α and the dispersion σ of each population are, in principle, free parameters. However, the low-luminosity portion of the LF is dominated by "cold" late-type galaxies and, as a consequence, the value of α of the warm population is largely unconstrained; we have fixed it at $\alpha_{warm} = 0.01$. In turn, the "warm" population dominates at high luminosities so that the data only imply an upper limit to σ_{cold}. We have set $\sigma_{cold} = 0.3$.

For the "warm" population, we have assumed power-law density and luminosity evolution [$\Phi^*(z) = \Phi_0^*(1+z)^{\alpha_\Phi}$; $L^*(z) = L_0^*(1 + z)^{\alpha_L}$] up to $z_{break} = 1$, α_Φ and α_L being free parameters. The "cold" population comprises normal disk galaxies for which chemo/spectrophotometric evolution models (Mazzei et al. 1992; Colavitti et al. 2008) indicate a mild (a factor $\simeq 2$ from $z = 0$ to $z = 1$) increase in the SFR, hence of IR luminosity, with look-back time. Based on these results we take, for this population, $\alpha_L = 1$ and no density evolution. At $z > z_{break}$ both $\Phi^*(z)$ and $L^*(z)$ are kept to the values at z_{break} multiplied by the smooth cutoff function $\{1 - \text{erf}[(z - z_{cutoff})/\Delta z)]\}/2$, with $z_{cutoff} = 2$ and $\Delta z = 0.5$. The choice of the redshift cutoff for both populations of late-type galaxies is motivated by the fact that the disk component of spirals and the irregular galaxies are characterized by relatively young stellar populations (formation redshift $z \lesssim 1$–1.5). Above $z = 1.5$, proto-spheroidal galaxies (including bulges of disk galaxies) dominate the contribution to the LF, at least in the observationally constrained luminosity range. The other parameters are determined by minimum χ^2 fits to selected data sets, as described in Section 5. Their best-fit values and the associated uncertainties are listed in Table 1.

Although there is clear evidence of systematic variations of the IR SEDs of low-z galaxies with luminosity (e.g., Smith et al. 2012), we tried to fit the data with just two SEDs, one for the "warm" and one for the "cold" population. These SEDs were generated by combining those of Dale & Helou (2002), which are best determined at mid-IR wavelengths, with those of Smith et al. (2012), primarily based on *Herschel* data in the range 100–500 μm. Dale & Helou (2002) give SED templates for several values of the 60–100 μm flux density ratio, $\log[f_\nu(60 \mu m)/f_\nu(100 \mu m)]$. Using the relation between this ratio and the 3–1100 μm luminosity, L_{TIR}, given by Chapman et al. (2003), we established a correspondence between their SEDs and those by Smith et al., labeled by the values of $\log(L_{IR}/L_\odot)$. The combined SEDs are based on Smith et al. above 100 μm and on Dale & Helou at shorter wavelengths. By trial and error, we found that the best fit to the data is obtained using for the "cold" population the SED corresponding to $\log(L_{IR}/L_\odot) = 9.75$ (actually the SEDs change very slightly for $\log(L_{IR}/L_\odot) \lesssim 9.75$) and for the "warm" population the SED corresponding to $\log(L_{IR}/L_\odot) = 11.25$. These two SEDs are displayed in Figure 4.

3.2. Reactivated AGNs

In the framework of our reference galaxy and AGN evolutionary scenario, most of the growth of supermassive black holes is associated with the star-forming phase of spheroidal components of galaxies at $z \gtrsim 1.5$ when the great abundance of ISM favors high accretion rates, at, or even slightly above, the Eddington limit. At later cosmic times the nuclei can be reactivated by, e.g., interactions, mergers, or dynamical instabilities. The accretion rates are generally strongly sub-Eddington. Our evolutionary scenario cannot predict their amplitudes and duty cycles. We therefore also adopted for these objects a phenomenological backward evolution model analogous to that used for the "warm" galaxy population, i.e., LFs of the same form of Equation (7) and power-law density and luminosity evolution with the same break and cutoff redshifts. However, the
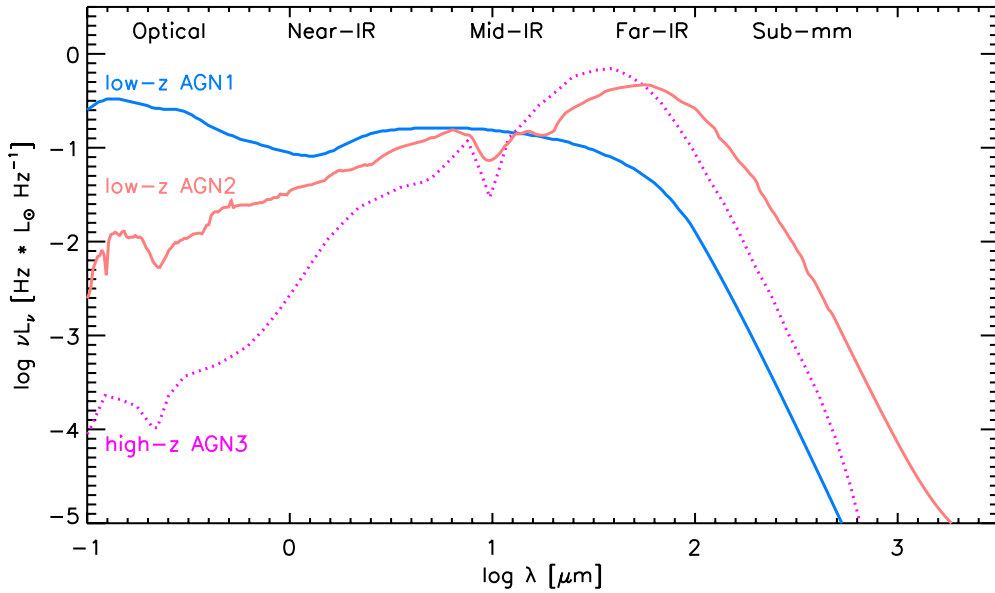
Figure 5. SEDs of low-z type 1 AGNs (solid light-blue line) and type 2 AGNs (solid pink line). The dotted magenta line shows, for comparison, the adopted SED of AGNs associated with dusty proto-spheroidal galaxies (type 3 AGNs). The SEDs are normalized to the same, arbitrary, bolometric luminosity.

(A color version of this figure is available in the online journal.)

Table 1
Parameters for Low-z AGNs and for "Warm" and "Cold" Galaxy Populations

	AGN 1 (12 μm)	AGN 2 (12 μm)	Warm (IR)	Cold (IR)
$\log(\Phi_0^*/\mathrm{Mpc}^{-3})$	-5.409 ± 0.098	-4.770 ± 0.122	-2.538 ± 0.051	-1.929 ± 0.112
$\log(L_0^*/L_\odot)$	9.561 ± 0.084	10.013 ± 0.093	10.002 ± 0.076	9.825 ± 0.087
α	1.1	1.5	0.01	1.372 ± 0.121
σ	0.627 ± 0.017	0.568 ± 0.021	0.328 ± 0.014	0.3
α_Φ	2.014 ± 0.400	4.499 ± 0.317	0.060 ± 0.200	0.0
α_L	2.829 ± 0.297	0.0	3.625 ± 0.097	1.0
z_{break}	1.0	1.0	1.0	1.0
z_{cutoff}	2.0	2.0	2.0	2.0

Notes. The parameters of the AGN luminosity functions refer to 12 μm (νL_ν), while those for galaxies refer to IR (8–1000 μm) luminosities. Values without error were kept fixed.

parameters of the LFs refer to 12 μm (see Section 3.1 and Table 1). The data do not allow a determination of the slopes, α, of the faint portions of the LFs. We have set $\alpha = 1.1$ for type 1 AGNs and $\alpha = 1.5$ for type 2. The steeper slope for type 2 was chosen on account of the fact that these dominate over type 1 at low luminosities. As in the case of normal late-type and of star-burst galaxies, the other parameters are obtained by minimum χ^2 fits, as detailed in Section 5, and the best-fit values are listed, with their uncertainties, in Table 1. For type 2 AGNs, pure density evolution was found to be sufficient to account for the data.

For type 1 AGNs we adopted the mean QSO SED by Richards et al. (2006), extended to millimeter wavelengths as described in Section 2.3, while for type 2 AGNs we adopted the SED of the local AGN-dominated ULIRG Mrk 231, taken from the SWIRE library (Polletta et al. 2007). These SEDs are shown in Figure 5, where the SED of type 3 AGNs associated with dusty star-forming proto-spheroidal galaxies is also plotted for comparison. The SED of type 3 AGNs is the most obscured at optical/near-IR wavelengths due to the effect of the dense, dusty ISM of the high-z host galaxies. This means that the counts at optical/near-IR wavelengths are dominated by type 1 AGNs with type 2 AGNs becoming increasingly important in the mid-IR. The three AGN populations have approximately the same ratio between the rest-frame 12 μm and

the bolometric luminosity, as first pointed out by Spinoglio & Malkan (1989).

The type 1/type 2 space density ratio yielded by the model increases with luminosity, consistent with observations (e.g., Burlon et al. 2011) and with the receding torus model (Lawrence 1991). In the framework of the standard unified model of AGNs type 1 and type 2 AGNs differ only in terms of the angle which the observers' line of sight makes with the axis of a dusty torus. If the line of sight to the central region is blocked by the torus, the AGN is seen as a type 2. According to the receding torus model, the opening angle of the torus (measured from the torus axis to the equatorial plane) is larger in more luminous objects, implying that obscuration is less common in more luminous AGNs. Since our model implies that type 1 AGNs (but not type 2's) are evolving in luminosity, they become increasingly dominant with increasing redshift.

4. SOURCE COUNTS AND CONTRIBUTIONS TO THE BACKGROUND

The surface density of sources per unit flux density and redshift interval is

$$\frac{d^3N(S_\nu, z)}{dS_\nu dz d\Omega} = \frac{\Phi(\log L_{\nu'}, z)}{L_{\nu'} \ln 10} \frac{dL_{\nu'}}{dS_\nu} \frac{d^2V}{dz d\Omega}, \qquad (8)$$

where $\nu' = \nu(1 + z)$,

$$S_\nu = \frac{(1 + z)L_{\nu'}}{4\pi D_{\rm L}^2(z)}, \qquad (9)$$

the comoving volume per unit solid angle is

$$\frac{d^2V}{dzd\Omega} = \frac{c}{H_0} \frac{(1 + z)^2 D_{\rm A}^2(z)}{E(z)}, \qquad (10)$$

and the luminosity distance $D_{\rm L}$ and the angular diameter distance $D_{\rm A}$ are related, in a flat universe, by

$$\frac{D_{\rm L}}{1 + z} = (1 + z)D_{\rm A} = \frac{c}{H_0} \int_0^z \frac{dz'}{E(z')}. \qquad (11)$$

The differential number counts, i.e., the number of galaxies with flux density in the interval $S_\nu \pm dS_\nu/2$ at an observed frequency ν per unit solid angle, are then

$$\frac{d^2N}{dS_\nu d\Omega}(S_\nu) = \int_{z_{\rm min}}^{z_{\rm max}} dz \frac{\Phi(\log L_{\nu'}, z)}{L_{\nu'} \ln 10} \frac{dL_{\nu'}}{dS_\nu} \frac{d^2V}{dzd\Omega}. \qquad (12)$$

The integral number counts, i.e., the number of galaxies with flux density $S_\nu > S_{\nu,{\rm inf}}$ at frequency ν per unit solid angle, are given by

$$\frac{dN}{d\Omega}(S_\nu > S_{\nu,{\rm inf}}) = \int_{z_{\rm min}}^{z_{\rm max}} dz \frac{d^2V}{dzd\Omega} \int_{\log L_{\nu',{\rm inf}}}^{\infty} \\ \times \Phi(\log L_{\nu'}, z)d\log L_{\nu'}, \qquad (13)$$

where $\nu' = (1 + z)\nu$ and $L_{\nu',{\rm inf}}$ is the monochromatic luminosity of a source at the redshift z observed to have a flux density $S_{\nu,{\rm inf}}$. Counts (per steradian) dominated by local objects ($z \ll 1$) can be approximated as

$$S_\nu^{2.5} \frac{d^2N}{dS_\nu d\Omega} \simeq \frac{1}{4\pi} \frac{1}{4\sqrt{\pi}} \int_0^{\infty} \Phi(\log L_\nu, z \simeq 0)L_\nu^{3/2}d\log L_\nu. \qquad (14)$$

The redshift distribution, i.e., the surface density of sources with observed flux densities greater than a chosen limit $S_{\nu,{\rm inf}}$ per unit redshift interval, is

$$\frac{d^2N}{dzd\Omega}(z, S_\nu > S_{\nu,{\rm inf}}) = \int_{S_{\nu,{\rm inf}}}^{\infty} \frac{d^3N}{dS_\nu' dzd\Omega}dS_\nu'. \qquad (15)$$

The steepness of the (sub-)millimeter counts of proto-spheroidal galaxies and their substantial redshifts imply that their counts are strongly affected by the magnification bias due to gravitational lensing (Blain 1996; Perrotta et al. 2002, 2003; Negrello et al. 2007):

$$\frac{d^3N_{\rm lensed}(S_\nu, z)}{d\log S_\nu dzd\Omega} = \int_\mu d\mu \frac{d^3N(S_\nu/\mu, z)}{d\log S_\nu dzd\Omega} \frac{dP(\mu|z)}{d\mu}, \qquad (16)$$

where $dP/d\mu$ is the amplification distribution that describes the probability for a source at redshift z to be amplified by factor μ. Here, we have approximated to unity the factor $1/\langle\mu\rangle$ that would have appeared on the right-hand side, as appropriate for large-area surveys (see Jain & Lima 2011).

We have computed $dP/d\mu$ using the SISSA model worked out by Lapi et al. (2012). The differential counts including the effect of lensing can be computed integrating Equation (16) over z. The effect of lensing on counts of other source popula-

tions and on proto-spheroidal counts at shorter wavelengths is small and will be neglected in the following.

Interesting constraints on the halo masses of proto-spheroidal galaxies come from the auto- and cross-correlation functions of intensity fluctuations. A key quantity in this respect is the flux function, $d^2S_\nu/dzd\Omega$, i.e., the redshift distribution of the cumulative flux density of sources below the detection limit $S_{\nu,{\rm lim}}$

$$\frac{d^2S_\nu}{dzd\Omega} = \int_0^{S_{\nu,{\rm lim}}} \frac{d^3N}{dS_\nu dzd\Omega}S_\nu dS_\nu. \qquad (17)$$

The contribution of a source population to the extragalactic background at the frequency ν is

$$I_\nu = \int_0^{\infty} S_\nu \frac{d^2N(S_\nu)}{dS_\nu d\Omega}dS_\nu. \qquad (18)$$

5. DETERMINATION OF THE BEST-FIT VALUES OF THE PARAMETERS

A minimum χ^2 approach for estimating the optimum values of the parameters of the physical model for proto-spheroidal galaxies and associated AGNs is unfeasible because of the lengthy calculations required. Some small adjustments compared to earlier versions (Granato et al. 2004; Lapi et al. 2006; Mao et al. 2007) were made, by trial and error, to improve the agreement with observational estimates of LFs at $z > 1.5$. An outline of the model, including the definition of the relevant parameters, is presented in the Appendix. The chosen values are listed in Table 2. Discussions of physically plausible ranges can be found in Granato et al. (2004), Cirasuolo et al. (2005), Lapi et al. (2006), Shankar et al. (2006), Cook et al. (2009), and Fan et al. (2010).

On the contrary, the minimum χ^2 approach was applied to late-type/starburst galaxies and to reactivated AGNs. The χ^2 minimization was performed using the routine *MPFIT*[9] exploiting the Levenberg–Marquardt least-squares method (Moré 1978; Markwardt 2009).

The huge amount of observational data in the frequency range of interest here and the large number of parameters coming into play forced us to deal with subsets of parameters at a time using specific data for each subset. The parameters of the evolving AGN LFs were obtained using:

1. the *B*-band local QSO LF of Hartwick & Schade (1990);
2. the *g*-band QSO LFs at $z = 0.55$ and 0.85 of Croom et al. (2009);
3. the $z \lesssim 0.75$, 1.24 μm AGN LFs of Assef et al. (2011);
4. the bright end [$\log(L_{60}/L_\odot) \geqslant 12$] of the local 60 μm LF of Takeuchi et al. (2003);
5. the *Spitzer* AGN counts at 8 and 24 μm of Treister et al. (2006).

The *B*- and *g*-band LFs were used to constrain the parameters of type 1 AGNs (type 2 being important only at the low-luminosity end), while the 1.24 μm LFs were regarded as made by a combination of type 1 and type 2 AGNs, the latter being dominant at low luminosities.

As for the evolving LFs of "warm" and "cold" galaxy populations we used the following data sets:

1. the *IRAS* 60 μm local LF of Soifer & Neugebauer (1991);
2. the *Planck* 350, 550, and 850 μm local LFs of Negrello et al. (2013);

---

9 http://purl.com/net/mpfit

Table 2
Parameters of the Physical Model for the Evolution of Proto-spheroidal Galaxies and Associated AGNs

Parameter	Value	Plausible Range	Description
τ_{RD}^0	3.0	1–10[a]	Normalization of optical depth of gas cloud (Equation (A9))
ϵ	0.10	0.06–0.42	Black hole accretion radiative efficiency (Equation (A16))
λ_{Edd}	1–4	$\lesssim$a few[b]	Redshift-dependent Eddington ratio (Equation (A14))
ϵ_{QSO}	3.0	1–10[a]	Strength of QSO feedback (Equation (A19))
$k_{\star,IR}$	3.1	2–4[c]	Conversion factor from SFR to IR luminosity (Equation (A7))
σ_*	0.10	$\lesssim$ 0.5	Dispersion of mean stellar luminosity (Equation (6))
$\sigma_\bullet$	0.35	$\lesssim$ 0.5[b]	Dispersion of mean AGN luminosity (Equation (6))
$f_{gas,crit}$	0.03	$\lesssim$ 0.165	Gas mass fraction at transition from obscured to unobscured AGNs (Section 2.2))
ϵ_{SN}	0.05	0.01–0.1[d]	Strength of SN feedback (Equation (A6))
α_{RD}	2.5	1–10[e]	Strength of radiation drag (Equation (A8))

Notes. The values of the first eight parameters used here are somewhat different from those used in previous papers, but are still well within the plausible ranges listed in Column 3 and discussed in the references given in the footnotes.
[a] Granato et al. (2004).
[b] Lapi et al. (2006).
[c] Lapi et al. (2011).
[d] Shankar et al. (2006).
[e] A. Lapi et al. (in preparation).

Table 3
References for Data on Number Counts (See Figure 13)

Wavelength (μm)	Instrument	Field	Reference
15, 24	*Akari*/IRC	NEP-deep	Takagi et al. (2012)
15	*Akari*/IRC	De-lensed A2218	Hopwood et al. (2010)
15	*Akari*/IRC	NEP-deep+wide	Pearson et al. (2010)
15	*Akari*/IRC	CDFS	Burgarella et al. (2009)
15	*Akari*/IRC	NEP-deep	Wada et al. (2007)
15	*ISO*/ISOCAM	ELAIS-S	Gruppioni et al. (2002)
15	*ISO*/ISOCAM	ISOCAM deep surveys	Elbaz et al. (1999)
16	*Spitzer*/IRS	GOODS-N+S	Teplitz et al. (2011)
24, 70	*Spitzer*/MIPS	ADF-S	Clements et al. (2011)
24, 70	*Spitzer*/MIPS	*Spitzer* legacy fields	Béthermin et al. (2010)
24	*Spitzer*/MIPS	SWIRE fields	Shupe et al. (2008)
24	*Spitzer*/MIPS	NDWFS Bootes	Brown et al. (2006)
24	*Spitzer*/MIPS	GOODS-N	Treister et al. (2006)
24	*Spitzer*/MIPS	Deep *Spitzer* fields	Papovich et al. (2004)
70, 100	*Herschel*/PACS	GOODS, LH, COSMOS	Berta et al. (2011)
70	*Spitzer*/MIPS	xFLS	Frayer et al. (2006)
70	*Spitzer*/MIPS	Bootes, Marano, CDF-S	Dole et al. (2004)
100	*Herschel*/PACS	A2218	Altieri et al. (2010)
250, 500	*Herschel*/SPIRE	HerMES	Béthermin et al. (2012b)
250, 500	*Herschel*/SPIRE	H-ATLAS	Clements et al. (2010)
250, 500	*Herschel*/SPIRE	HerMES	Oliver et al. (2010)
250, 500	*Herschel*/SPIRE	HerMES P(D)	Glenn et al. (2010)
250, 500	BLAST	BGS P(D)	Patanchon et al. (2009)
500	*Herschel*/SPIRE	H-ATLAS	Lapi et al. (2012)
550, 850	*Planck*	*Planck* all-sky survey	Planck Collaboration (2013)
850	SCUBA	Clusters	Noble et al. (2012)
850	SCUBA	A370	Chen et al. (2011)
850	SCUBA	Clusters	Zemcov et al. (2010)
850	SCUBA	Clusters and NTT-DF	Knudsen et al. (2008)
850	SCUBA	SHADES	Coppin et al. (2006)
850	SCUBA	Clusters	Smail et al. (2002)
870	APEX/LABOCA	Clusters	Johansson et al. (2011)
1100	ASTE/AzTEC	AzTEC blank-field survey	Scott et al. (2012)
1100	ASTE/AzTEC	COSMOS	Aretxaga et al. (2011)
1100	ASTE/AzTEC	ADF-S, SXDF, and SSA22	Hatsukade et al. (2011)
1100	ASTE/AzTEC	GOODS-S	Scott et al. (2010)
1100	JCMT/AzTEC	SHADES	Austermann et al. (2010)
1100	JCMT/AzTEC	COSMOS	Austermann et al. (2009)
1400	SPT	SPT survey	Vieira et al. (2010)
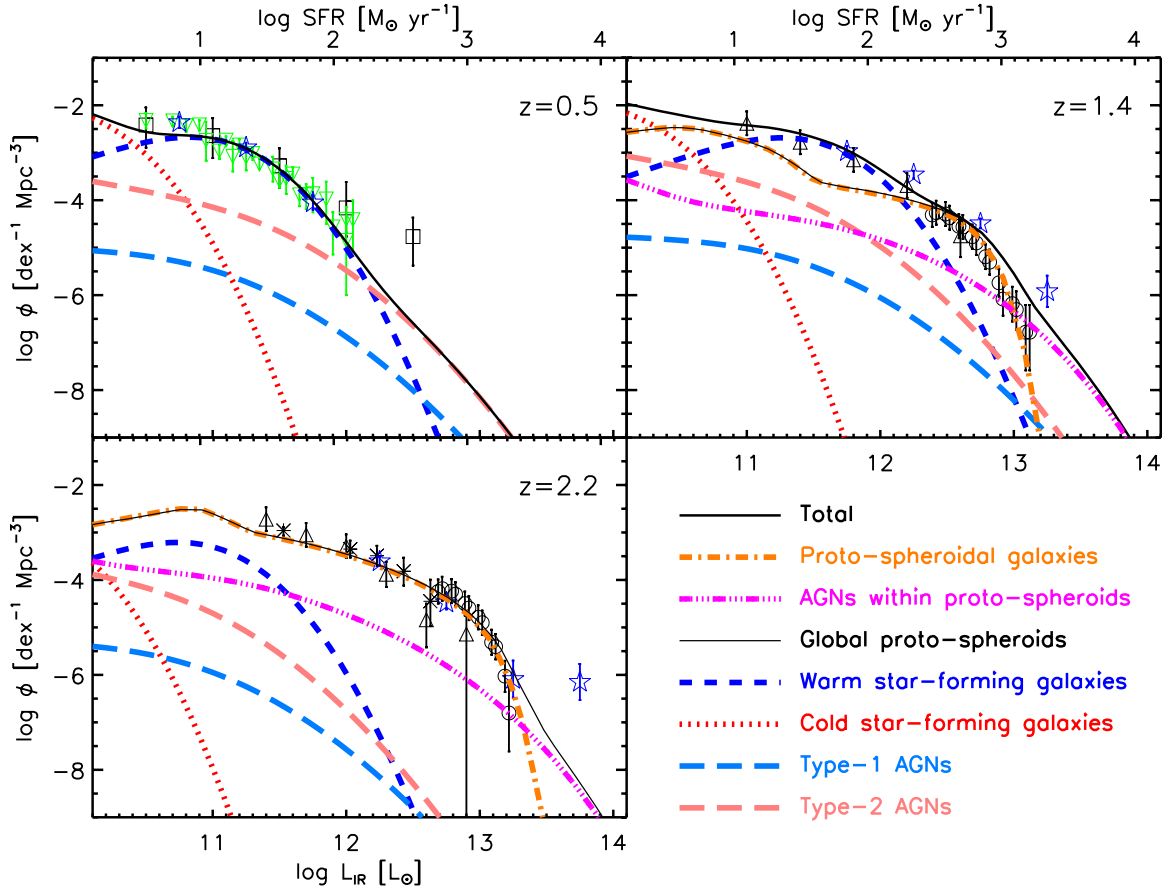
Figure 6. Comparison between model and observational determinations of the IR (8–1000 μm) luminosity functions at several redshifts. At $z > 1.0$, we have contributions from proto-spheroidal galaxies (dot-dashed orange lines) and from the associated AGNs (both obscured and unobscured; triple-dot-dashed magenta lines). The thin solid black lines (that are generally superimposed to the dot-dashed orange lines) are the combination of the two components. These contributions fade at lower redshifts and essentially disappear at $z < 1$. At $z \leqslant 1.5$, the dominant contributions come from "warm" (short-dashed blue lines) and "cold" (dotted red lines) star-forming galaxies. Type 2 AGNs (long-dashed pink lines) or type 3 AGNs associated with dusty proto-spheroids (triple-dot-dashed magenta lines) dominate at the highest IR luminosities, while type 1 AGNs (long-dashed light-blue lines) are always sub-dominant (in the IR). The thick solid black lines show the sum of all contributions. The upper horizontal scale gives an estimate of the SFRs corresponding to IR luminosities. These estimates are only indicative (see Section 6.1). Data points are from Le Floc'h et al. (2005; black open squares), Caputi et al. (2007; black stars), Magnelli et al. (2009; green downward triangles), Rodighiero et al. (2010; blue open asterisks), Magnelli et al. (2011; black triangles), and Lapi et al. (2011; black open circles).

(A color version of this figure is available in the online journal.)

3. the *Spitzer* MIPS counts at 24, 70, and 160 μm of Béthermin et al. (2010);

4. the *Herschel* PACS counts at 160 μm of Berta et al. (2011);

5. the *Herschel* SPIRE counts at 250, 350, and 500 μm (Béthermin et al. 2012b).

The fits of the counts were made after having subtracted the contributions of proto-spheroidal galaxies, which are only important at wavelengths $\geqslant 160$ μm. The best-fit values of the parameters are listed in Table 1, where values without errors denote parameters that were kept fixed, as mentioned in Section 3.

In comparing model results with observational data, the instrumental spectral responses were taken into account. This is especially important in the mid-IR because of the complexity of the SEDs due to PAH emission lines. The monochromatic luminosity at the effective frequency ν_{eff} in the observer's frame is given by

$$L(\nu_{\mathrm{eff}}) \equiv \int T(\nu') L_{\nu'(1+z)} d\nu' \Big/ \int T(\nu') d\nu', \quad (19)$$

where $T(\nu)$ is spectral response function and the integration is carried out over the instrumental bandpass. When the model is compared with LF data at frequency ν_i (in the source frame) coming from different instruments for sources at redshift z, we use the response function of the instrument for which ν_{eff} is closest to $\nu_i/(1 + z)$. In the case of source counts, we use the response function appropriate for the most accurate data.

6. RESULTS

6.1. Model versus Observed Luminosity Functions and Redshift Distributions

The most direct predictions of the *physical model* for proto-spheroidal galaxies are the redshift-dependent SFRs and accretion rates onto the supermassive black holes as a function of halo mass. During the dust enshrouded evolutionary phase, the SFRs can be immediately translated into the IR (8–1000 μm) LFs of galaxies. As mentioned above, according to our model, the transition from the dust obscured to the passive evolution phase is almost instantaneous and we neglect the contribution of passive galaxies to the IR LFs. In turn, the accretion rates
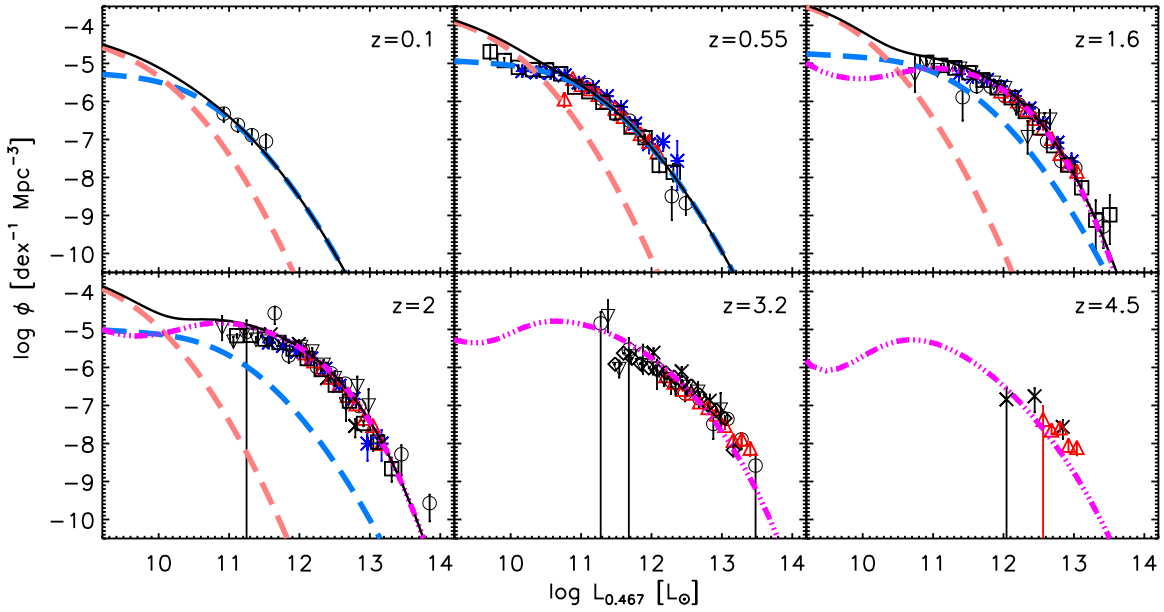
Figure 7. Comparison between model and observed g-band ($0.467\,\mu$m) AGN luminosity function at several redshifts. As in Figure 6 the long-dashed light-blue and pink lines refer to type 1 and type 2 AGNs, respectively, while the triple-dot-dashed magenta lines refer to AGNs associated with proto-spheroidal galaxies. At $z < 2$, the solid black line shows the sum of all the contributions. At higher z only proto-spheroids are considered. Data points are from Hartwick & Schade (1990; black open circles), Warren et al. (1994; black crosses), Croom et al. (2004; blue stars), Richards et al. (2006; red triangles), Croom et al. (2009; black open squares), Palanque-Delabrouille et al. (2013; black downward triangles), and Ross et al. (2012; black diamonds). The data by Hartwick & Schade (1990), given in terms of M_B in the Vega system, were converted to M_g adopting the $B - g \simeq 0.14$ color estimated by Fukugita et al. (1996) and were further corrected for the different cosmology. The UV magnitudes of Warren et al. (1994) were first converted to B magnitudes ($M_B = M_{C,1216\,\text{Å}} + 1.39\alpha_\nu + 0.09$, with $\alpha_\nu = -0.5$) following Pei (1995) and then to M_g as before. The data by Ross et al. (2012) were converted from $M_i(z = 2)$ to M_g following Richards et al. (2006) with spectral index $\alpha_\nu = -0.5$. The correction for the different cosmology was also applied. Finally, the conversion from M_g to $\nu L_\nu(0.467\,\mu$m) is given in Section 6.1.

(A color version of this figure is available in the online journal.)

translate into bolometric luminosities of AGNs given the mass-to-light conversion efficiency for which we adopt the standard value $\epsilon = 0.1$. The SEDs then allow us to compute the galaxy and AGN LFs at any wavelength.

In contrast, the *phenomenological model* for late-type/starburst galaxies yields directly the redshift-dependent IR LFs and that for reactivated AGNs yields the $12\,\mu$m LFs. Again these can be translated to any wavelength using the SEDs described in the previous sections.

In Figure 6, the model IR LFs are compared with observation-based determinations at different redshifts. At $z > 1.5$, the dominant contributions come from the stellar and AGN components of proto-spheroidal galaxies. These contributions fade at lower redshifts and essentially disappear at $z < 1$. The model implies that AGNs associated with proto-spheroidal galaxies are important only at luminosities higher than those covered by the Lapi et al. (2011) LFs which therefore have been converted to bolometric LFs using their galaxy SED, i.e., neglecting the AGN contribution, so that $\log(L_{\rm IR}/L_\odot) = \log(L_{100}/L_\odot) + 0.21$ and $\log(L_{\rm IR}/L_\odot) = \log(L_{250}/L_\odot) + 1.24$. At $z \leqslant 1.5$ "warm" and "cold" star-forming galaxies take over, "cold" galaxies being important only at low luminosities. Type 2 AGNs (long-dashed pink lines) may dominate at the highest IR luminosities, while type 1 AGNs (long-dashed light-blue lines) are always subdominant (in the IR).

The scale on the top x-axis in Figure 6 gives the SFRs corresponding to the IR luminosities

$$\log\left(\frac{L_{\rm IR}}{L_\odot}\right) = \log\left(\frac{\rm SFR}{M_\odot\ \rm yr^{-1}}\right) + 9.892, \qquad (20)$$

and is therefore meaningful only to the extent that the AGN contribution is negligible. Moreover, the normalization constant applies to high-z proto-spheroidal galaxies whose IR luminosity comes almost entirely from star-forming regions. For more evolved galaxies, older stellar populations can contribute significantly to the dust heating (da Cunha et al. 2012); therefore $L_{\rm IR}$ is no longer a direct measure of the SFR and therefore the upper scale has to be taken as purely indicative.

Observational determinations of LFs are available in many wave bands and for many cosmic epochs. The comparison between the model and the observed g-band ($0.467\,\mu$m) AGN LFs at several redshifts is presented in Figure 7, while the comparison in the J band ($1.24\,\mu$m) is shown in Figure 8. The conversion from monochromatic absolute AB magnitude $M_{\lambda,\rm AB}$ to the corresponding monochromatic luminosity $\nu L_\nu(\lambda)$ is given by $\log(\nu L_\nu/[L_\odot]) = -0.4M_{\lambda,\rm AB} - \log(\lambda/[\text{Å}]) + 5.530$. The contribution of type 2 AGNs at $z < 1.5$ strongly increases from the g to the J band. Apart from the low-luminosity portion of the J-band LF, very likely affected by incompleteness, the agreement between the model and the data is remarkably good.

The comparisons between the global (stellar plus AGN components) luminosity functions yielded by the model and those observationally determined at several redshifts and wavelengths are shown in Figures 9–11. In Figure 12, we compare model and observed redshift distributions at various wavelengths and flux density limits. The comparisons for all the other wavelengths for which estimates of the LF are available can be found in the Web site http://people.sissa.it/~zcai/galaxy_agn/.

Note that a substantial fraction of sources have only photometric redshifts. For example, the fraction of photometric redshifts is 91% for the VVDS-SWIRE survey with $S_{24\,\mu\rm m} > 0.4$ mJy
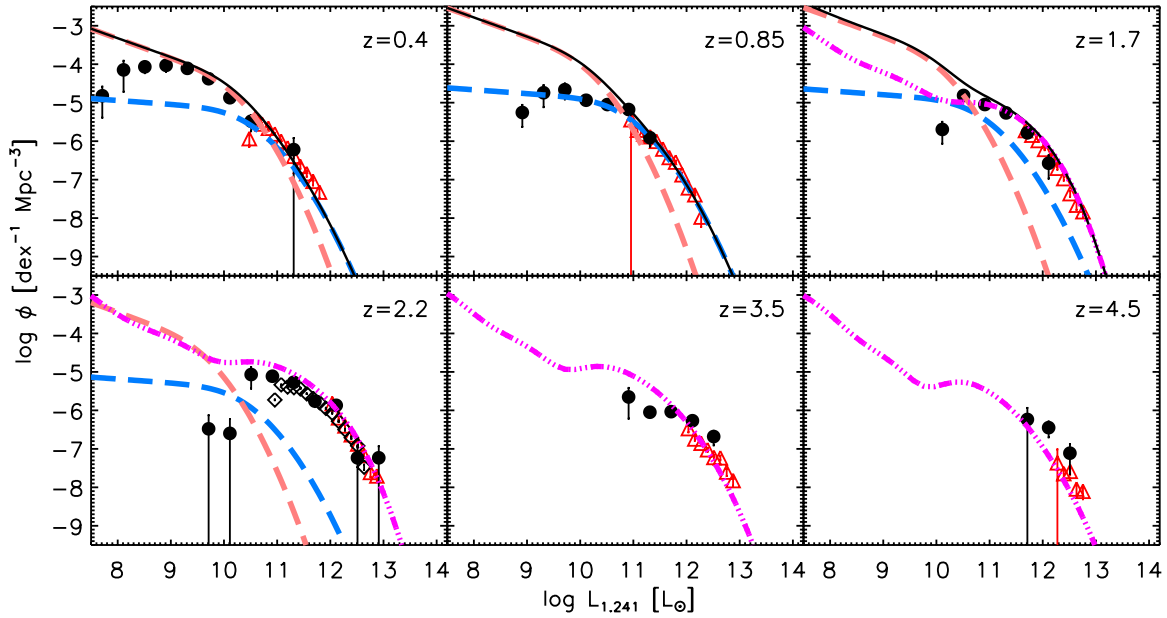
Figure 8. Comparison between model and observed *J*-band (1.24 μm) AGN luminosity function at several redshifts. The lines have the same meaning as in Figure 7. There are clear signs of substantial incompleteness at the lowest luminosities. Data are from Richards et al. (2006; red triangles), Assef et al. (2011; black filled circles), and Ross et al. (2012; black diamonds). The data by Assef et al. (2011), given in terms of M_J in the Vega system, were converted to $\nu L_\nu(1.241\ \mu m)$ using the relation ($L_\nu(1.241\ \mu m) = 1623 \times 10^{-0.4 M_J}$ Jy) by Rieke et al. (2008). The *i*-band data by Richards et al. (2006) and Ross et al. (2012) were converted to $M_{J,AB}$ assuming spectral index $\alpha_\nu = -0.5$.

(A color version of this figure is available in the online journal.)
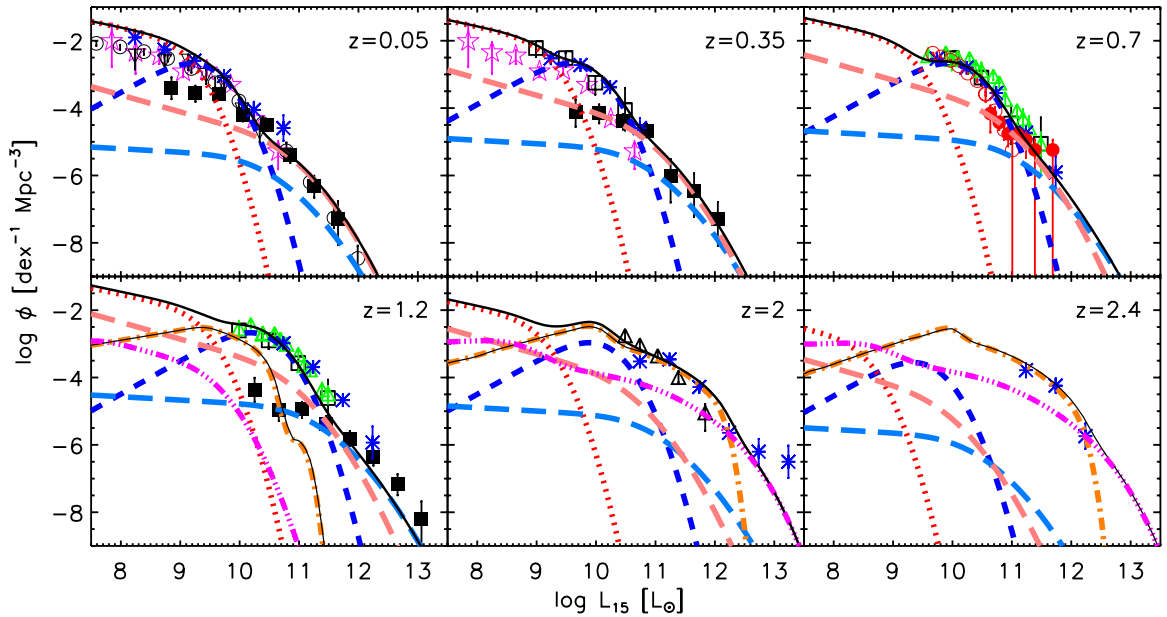
Figure 9. Comparison between model and observed 15 μm global (galaxies plus AGNs) luminosity function at several redshifts. Data are from Pozzi et al. (2004; magenta open asterisks), Le Floc'h et al. (2005, black open squares), Matute et al. (2006; black filled squares), Mazzei et al. (2007; black open circles), Magnelli et al. (2009, green triangles), Rodighiero et al. (2010; blue stars), Fu et al. (2010; red open circles for star formation and red filled circles for AGNs), Wu et al. (2011; black downward triangles), and Magnelli et al. (2011; black triangles). The black filled squares in the panels at $z = 0.05$ and 0.35 show observational estimates of the luminosity function of type 2 AGNs only, while the red filled circles at $z = 0.7$ refer to AGN of both types and at $z = 1.2$ refer to type 1 only. The lines have the same definition as in Figure 6.

(A color version of this figure is available in the online journal.)

(Rodighiero et al. 2010), 67.5% for the GOODS-N, and 36% for the GOODS-S samples with $S_{24\,\mu m} > 0.08$ mJy (Rodighiero et al. 2010). Only few sources at $z > 2$ have spectroscopic redshifts (Berta et al. 2011). Note that photometric redshift errors tend to moderate the decline of the distributions at high-z. The effect is analogous to the Eddington bias on source counts: errors move more objects from the more populated lower z bins

to the less populated higher z bins than in the other way. Thus, the observed distributions may be overestimated at the highest redshifts. In addition, optical identifications are not always complete. On the whole, observational estimates of LFs and of redshift distributions may be affected by systematic effects difficult to quantify and the true uncertainties may be larger than the nominal values.
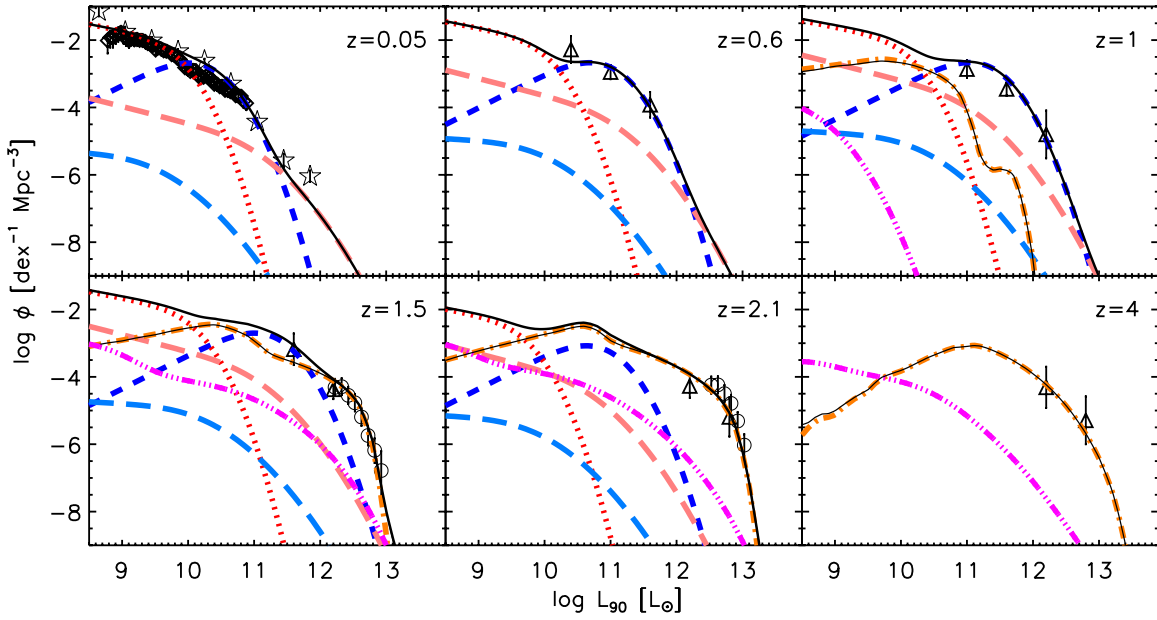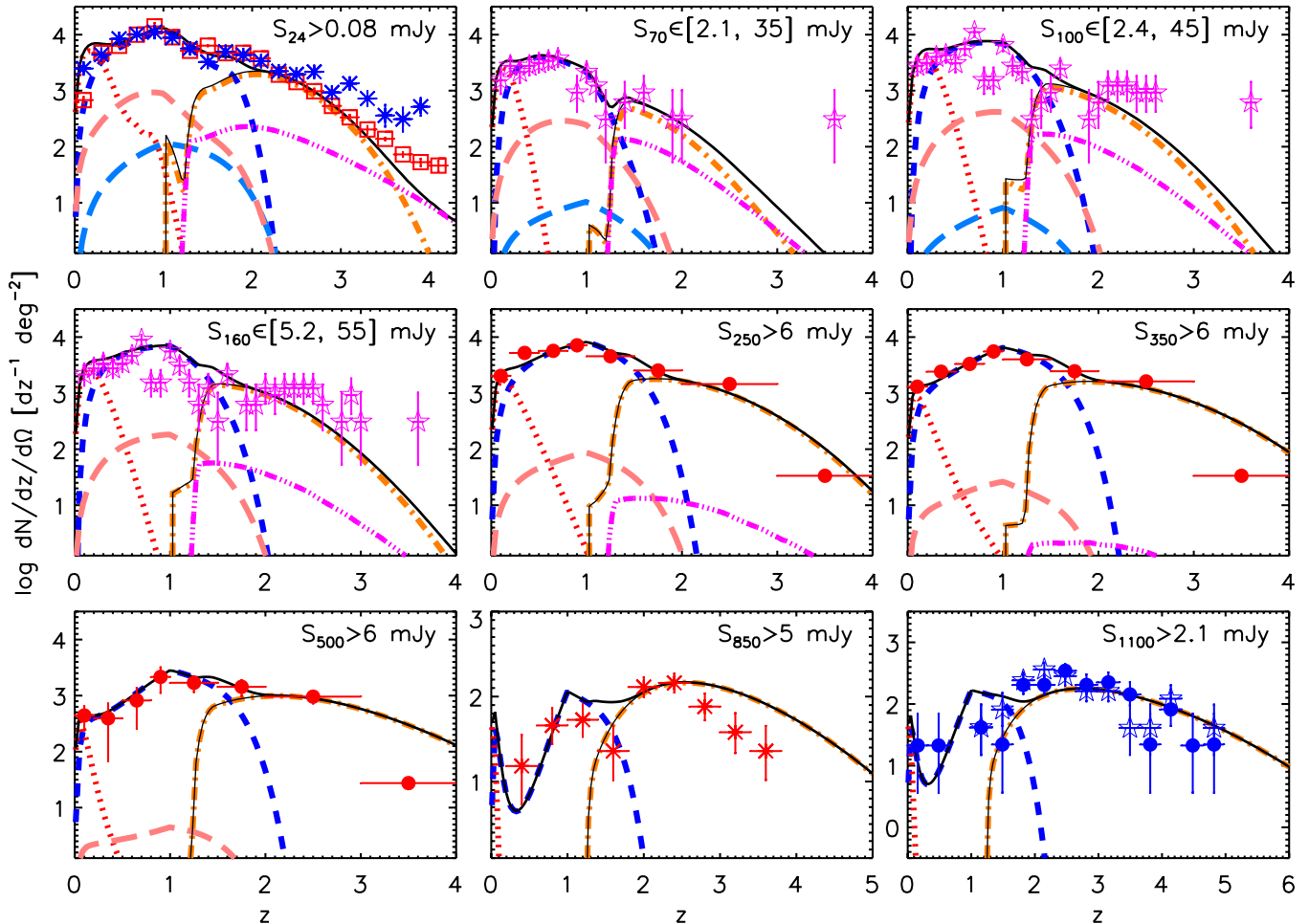
Figure 10. Comparison between model and observed 90 μm global (galaxies plus AGNs) luminosity function at several redshifts. The lines have the same definition as in Figure 6. Data are from Soifer & Neugebauer (1991; asterisks, 100 μm), Gruppioni et al. (2010; triangles), Sedgwick et al. (2011; diamonds), and Lapi et al. (2011; open circles, 100 μm).

(A color version of this figure is available in the online journal.)
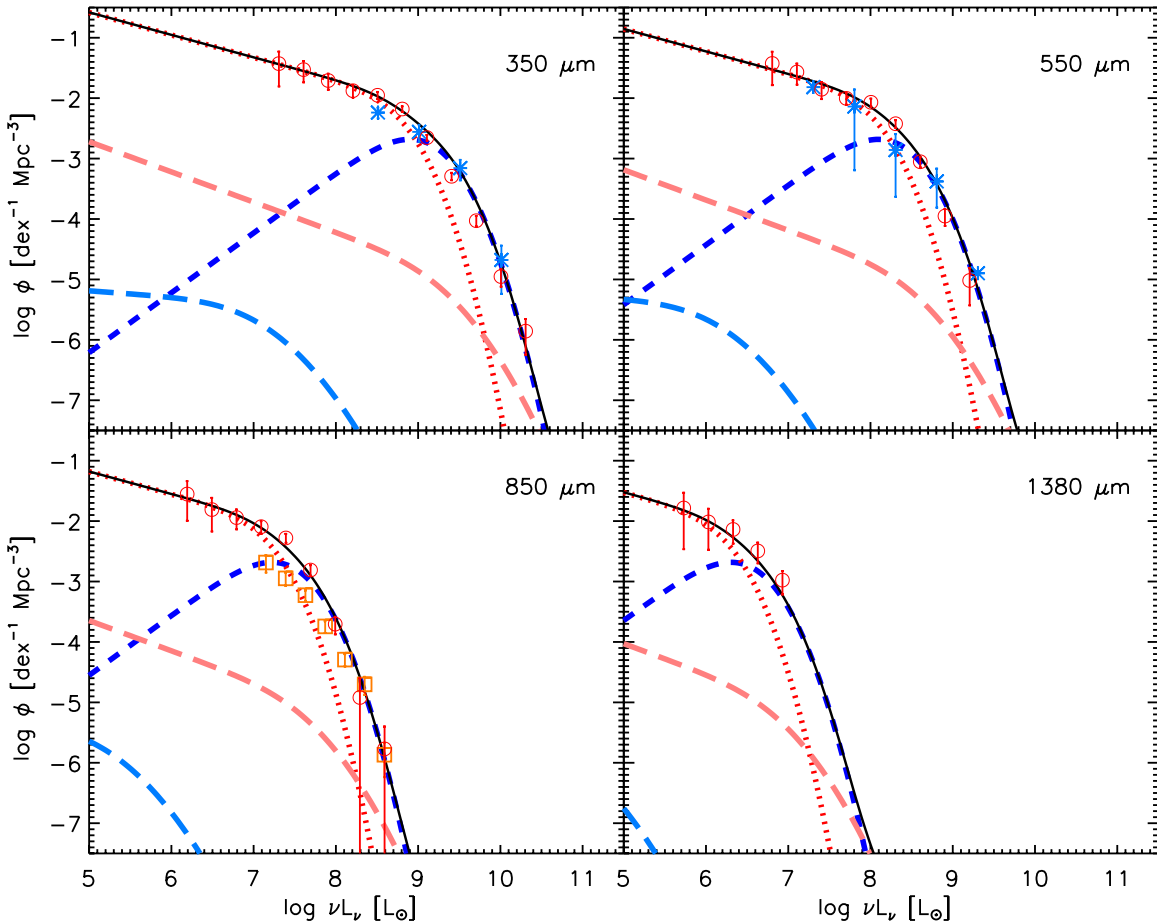
Figure 11. Local luminosity functions at (sub-)millimeter wavelengths. As in the other figures the short-dashed blue lines refer to "warm" galaxies, the dotted red lines to "cold" galaxies, the long-dashed pink lines to type 2 AGNs, and the long-dashed light-blue lines to type 1 AGNs. Data are from Dunne et al. (2000; orange open squares), Vaccari et al. (2010; light-blue stars), and Negrello et al. (2013; red open circles).

(A color version of this figure is available in the online journal.)

Figure 12. Comparison between model and observed redshift distributions at several wavelengths and for several flux density limits. The lines have the same definition as in Figure 6. Data are from Le Floc'h et al. (2009; red open squares, 24 μm), Rodighiero et al. (2010; blue stars, 24 μm), Berta et al. (2011; magenta open asterisks, 70, 100, and 160 μm), Béthermin et al. (2012b; red filled circles, 250, 350, and 500 μm), Chapman et al. (2005; red stars, 850 μm), and Yun et al. (2012; blue open asterisks based on the optical photo-z and blue filled circles based on millimetric photo-z). Note that a substantial fraction of sources have only photometric redshifts and only few $z > 2$ redshifts are spectroscopic. Photometric redshift errors tend to moderate the decline of the distributions at high-z; thus the observed distributions may be overestimated at the highest redshifts (see Section 6.1). The dip at $z \simeq 1.5$ in the observed redshift distribution of sources with $S_{850\,\mu m} > 5$ mJy is due to the "redshift desert," i.e., to the lack of strong spectral features within the observational window and the fast decline at $z > 2.5$ is due to the lack of radio identifications (Chapman et al. 2005). The dip around $z \simeq 1.5$ in the redshift distributions yielded by the model signals the transition from the phenomenological approach adopted for low-z sources to the physical approach for high-z proto-spheroidal galaxies and associated AGNs. Such artificial discontinuity is a weakness of the model that needs to be cleared by further work.

(A color version of this figure is available in the online journal.)

6.2. Model versus Observed Source Counts and Contributions to the CIB

Model and observed source counts at wavelengths from 15 μm to 1.38 mm are compared in Figure 13. At wavelengths $\geqslant$350 μm, where, in the present framework, proto-spheroidal galaxies are most important, the model provides a simple physical explanation of the steeply rising portion of the counts, which proved to be very hard to account for by other both physical (Hayward et al. 2013; Niemi et al. 2012; Lacey et al. 2010) and phenomenological (e.g., Béthermin et al. 2012a; Gruppioni et al. 2011) models.

In our model the sudden steepening of the (sub-)millimeter counts is due to the appearance of proto-spheroidal galaxies that show up primarily at $z \gtrsim 1.5$, being mostly in passive evolution at lower redshifts. Their counts are extremely steep because, due to the strongly negative K-correction, the submillimeter flux densities corresponding to a given luminosity are only weakly dependent on the source redshift. Then, since the

far-IR luminosity is roughly proportional to the halo mass, the counts reflect the high-z LF whose bright end reflects, to some extent, the exponential decline of halo mass function at high masses. This situation results in a very strong magnification bias due to gravitational lensing (Blain 1996; Perrotta et al. 2002, 2003; Negrello et al. 2007). The counts of strongly lensed galaxies depend on the redshift distribution of the unlensed ones. Thus, the good agreement between the model and the observed counts of strongly lensed galaxies (see the 350 μm, 500 μm, and 1380 μm panels of Figure 13) indicates that the model passes this test on the redshift distribution.

Low-z "warm" and "cold" star-forming galaxy populations become increasingly important with decreasing wavelength. At $\lambda \geqslant 160\,\mu$m, proto-spheroidal galaxies yield only a minor contribution to the counts. The AGN (mostly type 2) contribution implied by the model is always sub-dominant. We find a maximum contribution in the mid-IR. At 15 μm it is $\simeq$8% up to 1 mJy and then rapidly increases up to $\simeq$20% above 10 mJy, while at 24 μm it is $\simeq$7%–8% up to 0.5 mJy and increases up
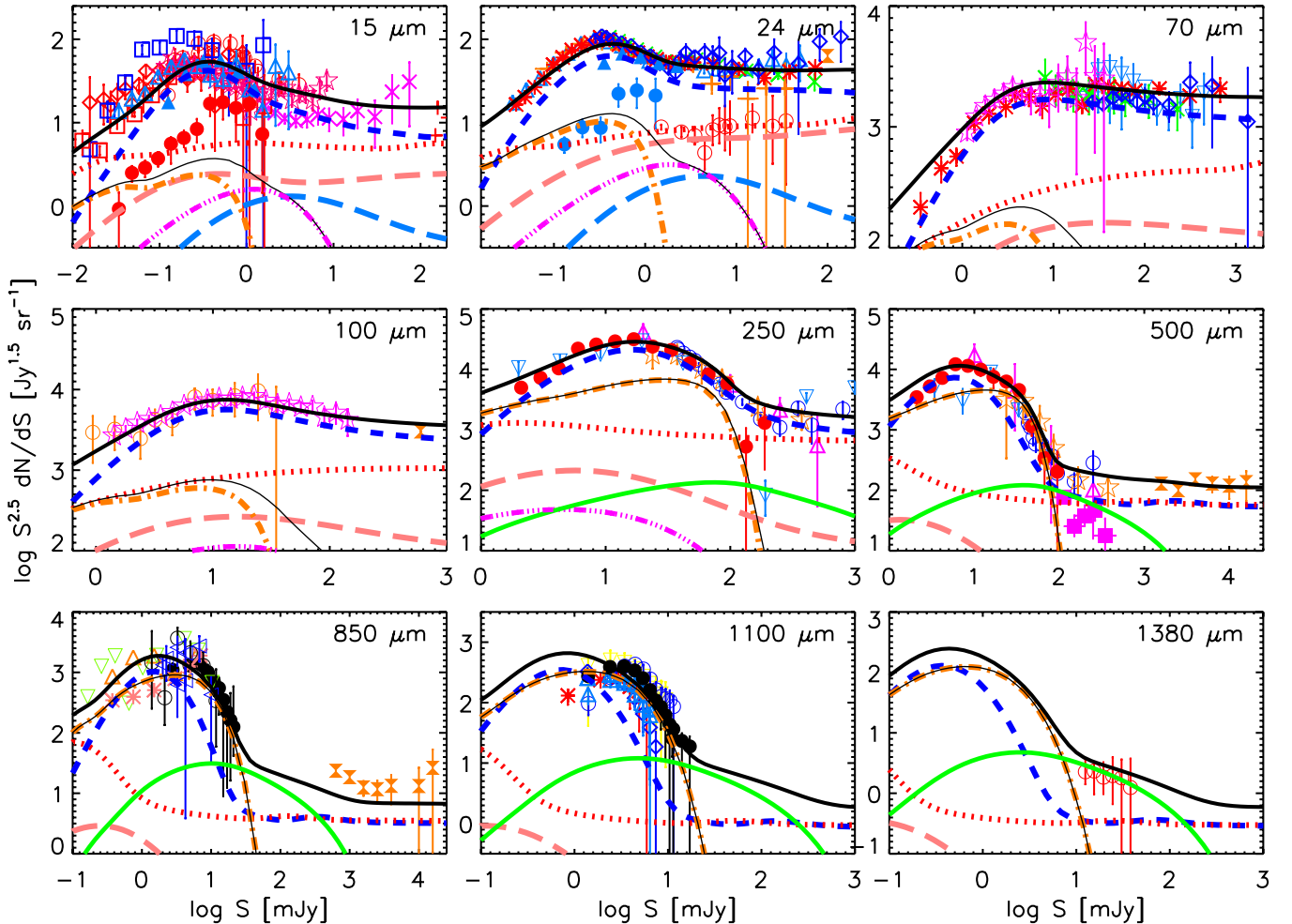
Figure 13. Euclidean normalized differential number counts at wavelengths from 15 μm to 1380 μm. The thick solid lines are the sum of contributions from: "cold" late-type galaxies (dotted red lines), "warm" (starburst) late-type galaxies (dashed blue lines), type 1 AGNs (long-dashed light-blue lines), type 2 AGNs (long-dashed pink lines), stellar component of proto-spheroids (dot-dashed orange lines), AGN component of proto-spheroids (triple-dot-dashed magenta lines), strongly lensed ($\mu \geqslant 2$) proto-spheroids (solid green lines; only significant at $\lambda \geqslant 250\,\mu$m). The thin solid black lines show the counts of unlensed proto-spheroids, including both the stellar and the AGN components; at $\lambda \geqslant 250\,\mu$m these counts essentially coincide with the counts of the stellar component only. The filled red circles in the 15 μm panel refer to AGNs only. The filled blue circles and the open red circles in the 24 μm panel refer to AGNs only and come from Treister et al. (2006) and Brown et al. (2006), respectively. The purple filled squares in the 500 μm panel show the estimated counts of strongly lensed galaxies (Lapi et al. 2012). The bright counts at 1.38 mm are also generally interpreted as due to strongly lensed galaxies (Vieira et al. 2010; Greve et al. 2012). References for all the data points are given in Table 3. The model provides a physical explanation of the sudden steepening of the (sub-)millimeter counts: it is due to the appearance of proto-spheroidal galaxies that show up primarily at $z \gtrsim 1.5$, being mostly in passive evolution at lower redshifts.

(A color version of this figure is available in the online journal.)

to $\simeq$20% above 2 mJy, in fair agreement with the observational estimates (Treister et al. 2006; Teplitz et al. 2011).

Another test on the redshift distribution is provided by the estimated counts in different redshift slices (Figure 14), although we caution that the true uncertainties may be larger than the nominal ones since the observational estimates are partly based on photometric redshifts and on stacking. The consistency between the model and the data is reasonably good.

Figure 15 shows the contributions of the different populations to the CIB. The model accounts for the full CIB intensity over the whole wavelength range. Only at $\lambda \leqslant 10\,\mu$m other galaxy populations, such as passively evolving galaxies, become important. According to the model, for $\lambda \geqslant 350\,\mu$m the main contribution to the CIB comes from proto-spheroidal galaxies and the fraction contributed by these objects increases with increasing wavelengths. Below $\lambda = 350\,\mu$m lower z "warm" galaxies take over, with "cold" galaxies adding a minor contribution. AGNs are always sub-dominant. The model gives a total (type

1+type 2+type 3) AGN contribution of 8.6% at 16 μm and of 8.1% at 24 μm. For comparison, Teplitz et al. (2011) estimate a contribution of $\sim$15% at 16 μm; Treister et al. (2006) and Ballantyne & Papovich (2007) find a contribution of $\sim$10% at 24 μm. It must be noted that these observational estimates are endowed with substantial uncertainties: on one side they may be too low because strongly obscured AGNs may be missed, and on the other side they may be too high because a significant fraction of the observed emission may come from the host galaxy.

7. CLUSTERING PROPERTIES OF DUSTY GALAXIES AND POWER SPECTRA OF THE COSMIC INFRARED BACKGROUND

An important test of our physical model for the evolution of dusty proto-spheroidal galaxies is provided by their clustering properties that are informative on their halo masses.
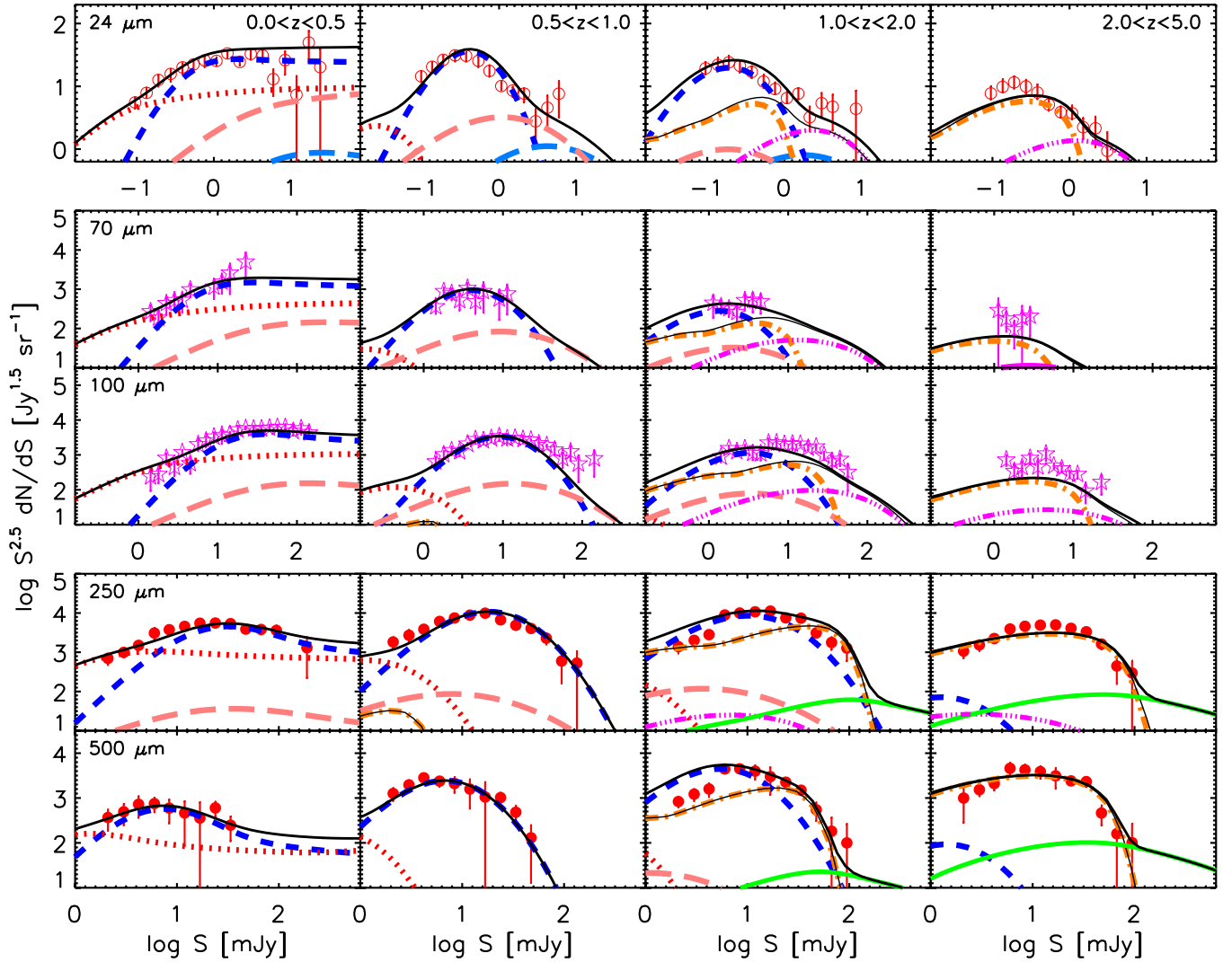
Figure 14. Euclidean normalized differential number counts per redshift slices. Lines have the same meaning as in Figure 13. Data are from Le Floc'h et al. (2009; red open circles, 24 μm), Berta et al. (2011; magenta open asterisks, 70 and 100 μm), and Béthermin et al. (2012b; red filled circles, 250 and 500 μm).

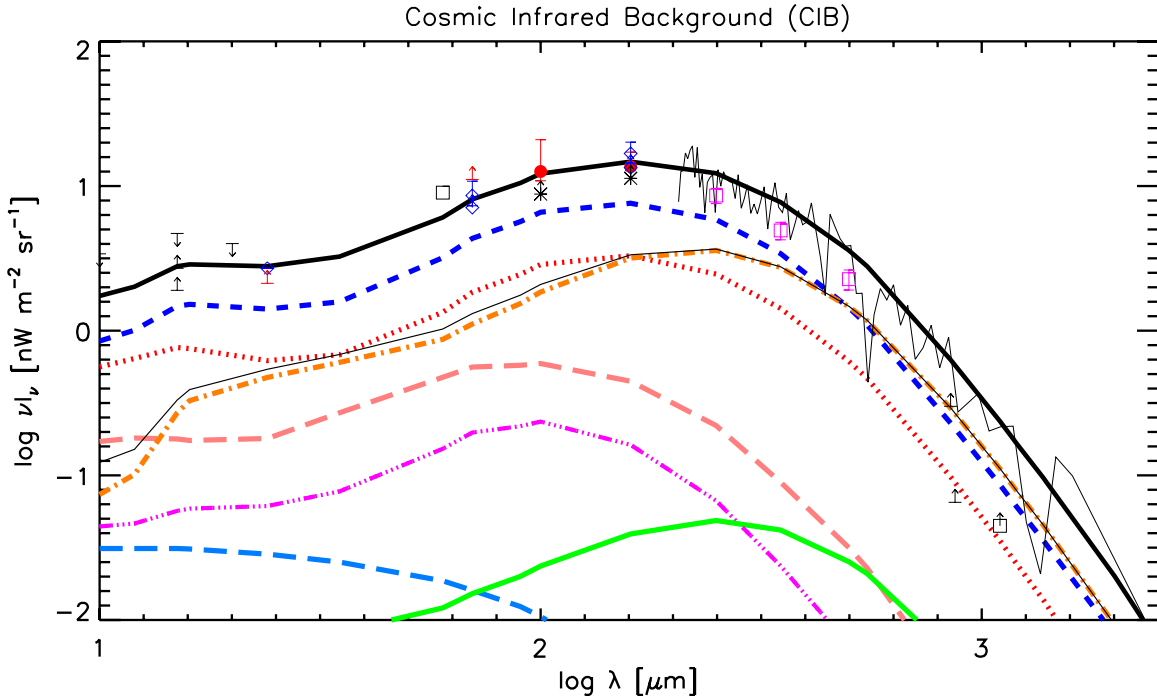(A color version of this figure is available in the online journal.)

A specific prediction of our model is that proto-spheroidal galaxies are the main contributors to the CIB at (sub-)millimeter wavelengths with "warm" starburst galaxies becoming increasingly important with decreasing wavelength. Since, in our model, proto-spheroidal galaxies are much more strongly clustered than starburst galaxies, the variation in the mixture with wavelength translates in quantitative predictions on the frequency dependence of the amplitude of the CIB power spectra and on the level of correlations among the maps at different frequencies.

We have updated the analysis by Xia et al. (2012) taking into account the new auto- and cross-frequency power spectra obtained by Viero et al. (2012) from *Herschel*/SPIRE measurements and the power spectrum at 100 μm derived by Pénin et al. (2012). The latter authors actually also give an estimate of the power spectrum at 160 μm. However, the amplitude of the latter is anomalously large. As an example, for the wavenumber $k_\theta = 0.03\,\mathrm{arcmin}^{-1}$ we find that the amplitude normalized to the CIB intensity,

$$\frac{\delta I}{I} = \frac{\left[2\pi k_\theta^2 P(k_\theta)\right]^{1/2}}{I_{\mathrm{CIB}}} \qquad (21)$$

(Equation (13) of Viero et al. 2012), is $\simeq 0.08$–0.09 at 100, 250, 350, and 500 μm but jumps to $\simeq 0.2$ at 160 μm. Since such a jump over a small wavelength range looks odd, we decided not to use the 160 μm power spectrum.

All the relevant details on the formalism used are given by Xia et al. (2012). Briefly, the power spectrum of the galaxy distribution is parameterized as the sum of the one-halo term that dominates on small scales and depends on the distribution of galaxies within the same halo, and the two-halo term that dominates on large scales and is related to correlations among different halos. The halo occupation distribution, which is a statistical description of how dark matter halos are populated with galaxies, is modeled using a central-satellite formalism (see, e.g., Zheng et al. 2005). This assumes that the first galaxy to be hosted by a halo lies at its center, while any remaining galaxies are classified as satellites and are distributed in proportion to the halo mass profile. The mean halo occupation function of satellite galaxies is parameterized as: $\langle N_{\mathrm{sat}} \rangle \propto (M_{\mathrm{vir}}/M_{\mathrm{sat}})^{\alpha_{\mathrm{sat}}}$, where M_{vir} is the halo mass and the power-law index α_{sat} is a free parameter. The key parameter in the two-halo term is the minimum halo mass, $M_{\mathrm{vir,min}}$, that determines the amplitude of the effective bias function $b_{\mathrm{eff}}(z)$.

Figure 15. Contributions of the different populations to the cosmic infrared background. The lines have the same meaning as in Figure 13. Proto-spheroidal galaxies are the main contributors to the CIB above $\simeq 500\,\mu m$. Data points are from Renault et al. (2001), Stecker & de Jager (1997), Lagache et al. (1999), Elbaz et al. (2002), Miville-Deschênes et al. (2002), Smail et al. (2002), Papovich et al. (2004), Dole et al. (2006), Marsden et al. (2009), Hopwood et al. (2010), Greve et al. (2010), Scott et al. (2010), Altieri et al. (2010), and Berta et al. (2011).

(A color version of this figure is available in the online journal.)

In the Xia et al. (2012) paper the only free parameters are the minimum halo mass, $M_{\mathrm{min,protosph}}$, and the power-law index of the mean occupation function of satellites, $\alpha_{\mathrm{sat,protosph}}$, of proto-spheroidal galaxies. This is because the contribution of late-type galaxies to the power spectra at $\lambda \geqslant 250\,\mu m$ is always sub-dominant and therefore the parameters characterizing their clustering properties were poorly constrained. This is no longer true if we add the $100\,\mu m$ power spectrum, which, however, still provides only weak constraints on $\alpha_{\mathrm{sat,late-type}}$. We therefore fixed that parameter to $\alpha_{\mathrm{sat,late-type}} = 1$. The fits to the *Herschel*/SPIRE power spectra determined by Viero et al. (2012) give $\log(M_{\mathrm{min,protosph}}/M_{\odot}) = 12.15 \pm 0.04$ and $\alpha_{\mathrm{sat,protosph}} = 1.55 \pm 0.05$ (1σ errors), close to the values found by Xia et al. (2012). The $100\,\mu m$ data do not constrain these parameters further but yield $\log(M_{\mathrm{min,late-type}}/M_{\odot}) = 11.0 \pm 0.06$. The nominal errors on each parameter have been computed marginalizing on the other and correspond to $\Delta\chi^2 = 1$. We caution that the true uncertainties are likely substantially higher than the nominal values, both because the model relies on simplifying assumptions that may make it too rigid and because of possible systematics affecting the data. Our value of $M_{\mathrm{min,protosph}}$ implies an effective halo mass (Equation (17) of Xia et al. 2012) at $z \simeq 2$ of proto-spheroidal galaxies, making up most of the CIB, $M_{\mathrm{eff}} \simeq 4.5 \times 10^{12}\,M_{\odot}$. This value is close to the estimated halo mass of the most effective star formers in the universe. Tacconi et al. (2008) estimated their mean comoving density at $z \sim 2$ to be $\sim 2 \times 10^{-4}\,\mathrm{Mpc}^{-3}$. For the standard ΛCDM cosmology, this implies that they are hosted by dark matter halos of $\sim 3.5 \times 10^{12}\,M_{\odot}$.

The best-fit model power spectra are plotted in Figure 16 where the one- and two-halo contributions of proto-spheroidal and late-type galaxies are also shown. The relative contribution of the latter galaxy population increases with decreasing

wavelength and becomes dominant at $100\,\mu m$. This trend implies a decrease of the level of correlations among the maps with increasing separation in wavelength. As illustrated by Figure 17, the model is in very good agreement with the cross-wavelength correlations measured by Viero et al. (2012) and defined by (Equation (14) of Viero et al. 2012)

$$C_{A \times B} = \frac{P_{k_\theta}^{A \times B}}{\sqrt{P_{k_\theta}^A \cdot P_{k_\theta}^B}}. \tag{22}$$

8. SUMMARY AND CONCLUSIONS

Studies of galaxy properties as a function of morphological type (e.g., Bernardi et al. 2010) have highlighted a dichotomy between the luminosity-weighted ages of early- and late-type galaxies. The former are mostly older than 8 Gyr while most of Sb or later-type spirals are younger than 7 Gyr, corresponding to a formation redshift $z \lesssim 1$–1.5. Building on this datum, we have worked out a model whereby the proto-spheroidal galaxies, in the process of forming the bulk of their stars, are the dominant population in the IR at $z \gtrsim 1.5$ while late-type galaxies dominate at lower redshifts. The model is "hybrid" in the sense that it combines a physical, forward model for spheroidal galaxies and the early evolution of the associated AGNs with a phenomenological backward model for late-type galaxies and for the later AGN evolution.

To describe the cosmological evolution of proto-spheroidal galaxies and of the associated AGNs, we adopted the physical model by Granato et al. (2004), upgraded working out, for the first time, the epoch-dependent LFs of sources as a whole (stellar plus AGN component), taking into account in a self-consistent way the variation with galactic age of the global SED.
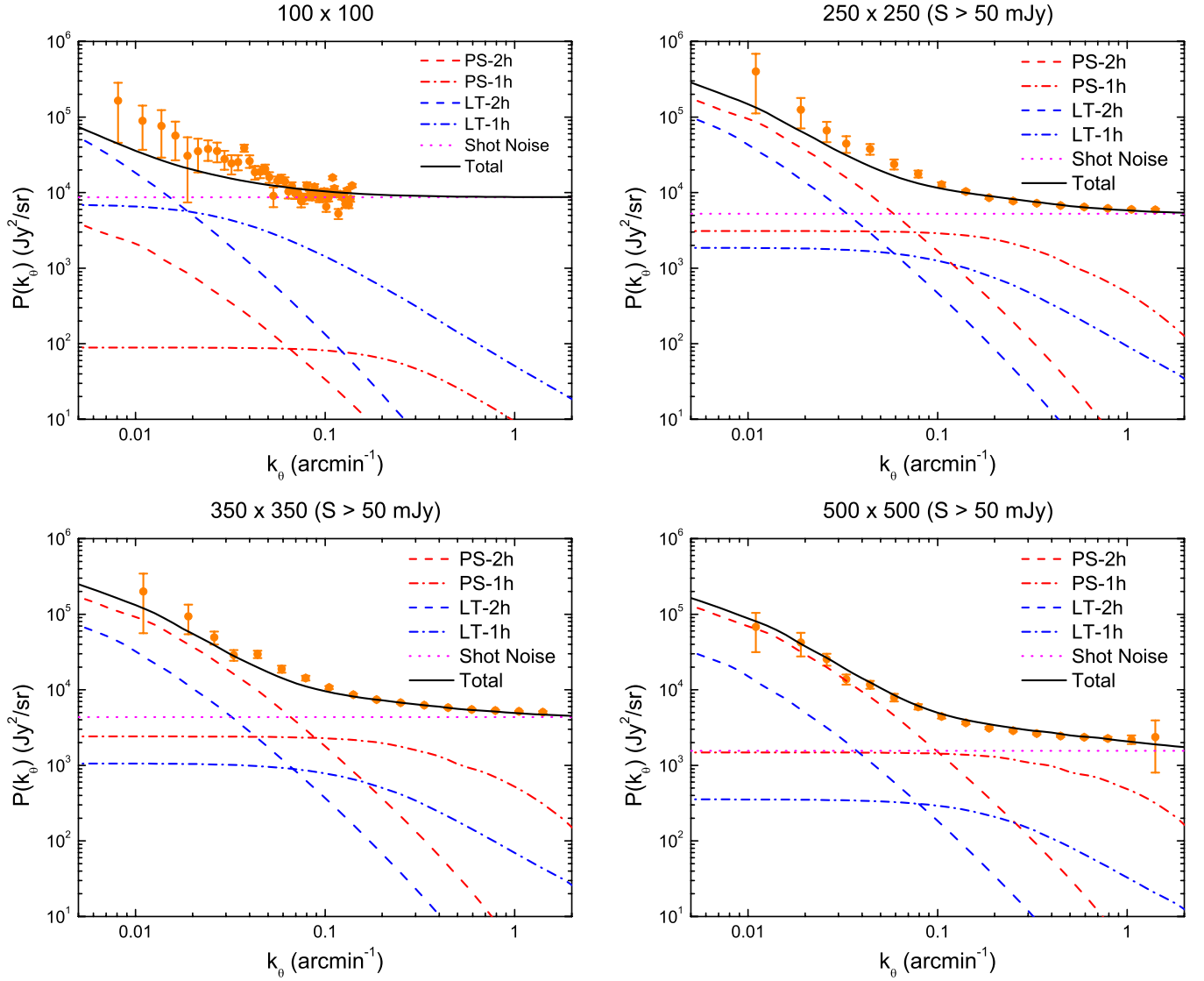
Figure 16. CIB angular power spectra at far-IR/submillimeter wavelengths. The $100\,\mu$m data are from Pénin et al. (2012), and those at longer wavelengths are from Viero et al. (2012). The lines show the contributions of the one-halo and two-halo terms for the two populations considered here: late-type (LT) "warm" plus "cold" galaxies and proto-spheroidal (PS) galaxies. The horizontal dotted magenta lines denote the shot noise level. At $\lambda \geqslant 250\,\mu$m, the signal is dominated by proto-spheroidal galaxies while late-type galaxies take over at shorter wavelengths.

(A color version of this figure is available in the online journal.)
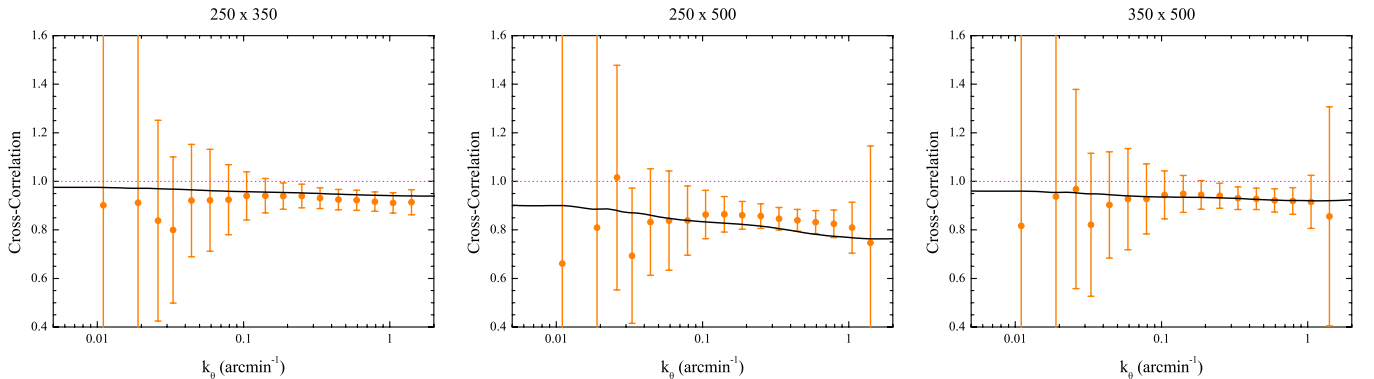
Figure 17. CIB cross-frequency power spectra at submillimeter wavelengths normalized according to Equation (14) of Viero et al. (2012). The solid line is the result from the model. The data are from Viero et al. (2012).

(A color version of this figure is available in the online journal.)

With only minor adjustments of the parameters, the model accurately reproduces the observed LFs at all redshifts ($z \gtrsim 1.5$) and IR wavelengths at which they have been determined. The model naturally accounts for the observed positive evolution of both galaxies and AGNs up to $z \simeq 2.5$ and for the negative evolution at higher redshifts. This is the result of the combination of two competing effects. On one side cooling and free-fall timescales shorten with increasing redshift because of the increase of the matter density and this yields higher SFRs, i.e., higher galaxy luminosities at given halo mass. The higher gas densities are also responsible for a delay of the AGN switch-off time by feedback implying positive luminosity and density evolution of these objects. These effects are thwarted by the decrease in the comoving density of massive halos that prevails above $z \simeq 2.5$ causing a decline of the bolometric LFs of both galaxies and AGNs.

The model also provides a simple physical explanation of the steeply rising portion of the (sub-)millimeter counts, which proved to be very hard to account for by other physical and phenomenological models. The sharp steepening is due to the sudden appearance of proto-spheroidal galaxies that do not have, in this spectral band, an evolutionary connection with nearby galaxies because their descendants are in passive evolution at $z \lesssim 1.5$. Their (sub-)millimeter counts are extremely steep because, due to the strongly negative K-correction, the flux densities corresponding to a given luminosity are only weakly dependent on the source redshift. Then, since the far-IR luminosity is roughly proportional to the halo mass, the counts reflect, to some extent, the exponential decline of halo mass function at high masses.

The steepness of the counts implies a strong magnification bias due to gravitational lensing. The counts of strongly lensed sources depend on the redshift distribution that determines the distribution of lensing optical depths. In fact, this model was the only one that correctly predicted (Negrello et al. 2007) the strongly lensed counts at $500\,\mu$m and the correct redshift distribution of bright ($S_{500\,\mu\text{m}} \geqslant 100$ mJy) submillimeter sources (Negrello et al. 2010; González-Nuevo et al. 2012).

The epoch-dependent LF of late-type galaxies has been modeled in terms of two populations, "warm" and "cold" galaxies with different SEDs and different evolution properties. Simple truncated power-law models have been adopted for the evolution of these populations. "Cold" (normal) late-type galaxies evolve (weakly) only in luminosity, while "warm" (starburst) galaxies evolve both in luminosity and in density.

Below $z = 1.5$, the far-IR emission of proto-spheroidal galaxies and the associated AGNs fade out rather rapidly. The AGNs, however, can be reactivated, e.g., by interactions. This later phase of AGN emission has been described by a phenomenological model analogous to that used for late-type galaxies, distinguishing between type 1 and type 2 AGNs.

In this framework, there is a systematic variation with wavelength of the populations dominating the counts and the contributions to the extragalactic background intensity. Above $350\,\mu$m the main contributors to the CIB are proto-spheroidal galaxies. In this wavelength range, late-type galaxies dominate the counts only at the brightest (where normal "cold" star-forming galaxies prevail) and at the faintest flux densities (where "warm" starburst galaxies outnumber the proto-spheroids). But these galaxies become increasingly important with decreasing wavelength. Proto-spheroids are always sub-dominant below $250\,\mu$m. This strong variation with wavelength in the composition of IR sources implies specific predictions for the auto- and

cross-power spectra of the source distribution, which may help discriminate between different models. Essentially, all the alternative models have all source populations present over the full relevant redshift range. This implies a high correlation between the CIB intensity fluctuations at different frequencies. On the contrary, the present model predicts a high (close to unity) cross-correlation only at the longest wavelengths ($\geqslant 500\,\mu$m). At shorter wavelengths the cross-correlation progressively weakens and we expect little cross-correlation between CIB fluctuations at, say, 100 and $500\,\mu$m. No observational determination is available for correlations among these wavelengths, but in the *Herschel*/SPIRE wavelength range, where cross-correlations have been measured, the model results are in good agreement with observations.

According to our model, the AGN contribution to the CIB is always sub-dominant. It is maximal in the mid-IR, where it reaches 8.6% at $16\,\mu$m and 8.1% at $24\,\mu$m. These contributions are close to, but somewhat lower than, most observation-based estimates which, however, are complicated by the difficulty of separating the AGN emission from that of the host galaxy. The AGN contribution to the counts is also always sub-dominant. We find a maximum contribution in the mid-IR where the model gives AGN fractions in fair agreement with the observational estimates (Treister et al. 2006; Teplitz et al. 2011).

APPENDIX

SELF-REGULATED EVOLUTION OF HIGH-z PROTO-SPHEROIDAL GALAXIES

The gas initially associated with a galactic halo of mass M_{vir}, with a cosmological mass fraction $f_{\text{b}} = M_{\text{gas}}/M_{\text{vir}} = 0.165$ is heated to the virial temperature at the virialization redshift, z_{vir}. Its subsequent evolution partitions it in three phases: a hot diffuse medium with mass M_{inf} infalling and/or cooling toward the center; cold gas with mass M_{cold} condensing into stars; low angular momentum gas with mass M_{res} stored in a reservoir around the central supermassive black hole, and eventually viscously accreting onto it. In addition, two condensed phases appear and grow, namely, stars with a total mass $M_{\star}$ and the black hole with mass $M_{\bullet}$. As mentioned in Section 2.1, we restrict ourselves to the ranges $11.3 \lesssim \log(M_{\text{vir}}/M_{\odot}) \lesssim 13.3$ and $z_{\text{vir}} \gtrsim 1.5$.

The evolution of the three gas phases is governed by the following equations:

$$\dot{M}_{\text{inf}} = -\dot{M}_{\text{cond}} - \dot{M}_{\text{inf}}^{\text{QSO}},$$
$$\dot{M}_{\text{cold}} = \dot{M}_{\text{cond}} - [1 - \mathcal{R}(t)]\dot{M}_{\star} - \dot{M}_{\text{cold}}^{\text{SN}} - \dot{M}_{\text{cold}}^{\text{QSO}}, \quad \text{(A1)}$$

$$\dot{M}_{\rm res} = \dot{M}_{\rm inflow} - \dot{M}_{\rm BH},$$

which link the mass infall rate, $\dot{M}_{\rm inf}$, the variation of the cold gas mass, $\dot{M}_{\rm cold}$, and the variation of the reservoir mass, $\dot{M}_{\rm res}$, to the condensation rate of the cold gas, $\dot{M}_{\rm cond}$, to the SFR $\dot{M}_\star$, to the cold gas removal by SN and AGN feedback, $\dot{M}_{\rm cold}^{\rm SN}$ and $\dot{M}_{\rm cold}^{\rm QSO}$, respectively, to the fraction of gas restituted to the cold component by the evolved stars, $\mathcal{R}(t)$, to the inflow rate of cold gas into the reservoir around the central supermassive black hole, $\dot{M}_{\rm inflow}$, and to the back hole accretion rate, $\dot{M}_{\rm BH}$.

The hot gas cools and flows toward the central region at a rate

$$\dot{M}_{\rm cond} \simeq \frac{M_{\rm inf}}{t_{\rm cond}}, \tag{A2}$$

with $M_{\rm inf}^0 = f_{\rm b} M_{\rm vir}$ and

$$t_{\rm cond} \simeq 8 \times 10^8 \left(\frac{1+z}{4}\right)^{-1.5} \left(\frac{M_{\rm vir}}{10^{12} M_\odot}\right)^{0.2} {\rm yr}, \tag{A3}$$

where the coefficient is 10% smaller than the value used by Fan et al. (2010). Note that the cooling and inflowing gas we are dealing with is the one already present within the halo at virialization. In this respect it is useful to keep in mind that the virial radius of the halo ($R_{\rm vir} \simeq 220(M_{\rm vir}/10^{13} M_\odot)^{1/3}[3/(1 + z_{\rm vir})]$ kpc) is more than 30 times larger than the size of the luminous galaxy, and that only a minor fraction of the gas within the halo condenses into stars. Indeed, we need strong feedback processes, capable of removing most of the halo gas, to avoid an overproduction of stars. This implies that any gas infalling from outside the halo must also be swept out by feedback; it could, however, become important for the formation of a disk-like structure surrounding the preformed spheroid once it enters the passive evolution phase, with little feedback (Cook et al. 2009). As mentioned in Section 2.1, the additional material (stars, gas, dark matter) infalling after the fast collapse phase that creates the potential well, i.e., during the slow-accretion phase, mostly produces a growth of the halo outskirts, and has little effect on the inner part where the visible galaxy resides.

The SFR is given by

$$\dot{M}_\star \simeq \frac{M_{\rm cold}}{t_\star}, \tag{A4}$$

where the star formation timescale is $t_\star \simeq t_{\rm cond}/s$ with $s \simeq 5$. For a Chabrier (2003) IMF of the form $\phi(m) = m^{-x}$ with $x = 1.4$ for $0.1 \leqslant m \leqslant 1 M_\odot$ and $x = 2.35$ for $m > 1 M_\odot$, we find $\mathcal{R} \simeq 0.54$ under the instantaneous recycling approximation.

The gas mass loss due to the SN feedback is

$$\dot{M}_{\rm cold}^{\rm SN} = \beta_{\rm SN} \dot{M}_\star, \tag{A5}$$

with

$$\beta_{\rm SN} = \frac{N_{\rm SN} \epsilon_{\rm SN} E_{\rm SN}}{E_{\rm bind}} \simeq 0.6 \left(\frac{N_{\rm SN}}{8 \times 10^{-3}/M_\odot}\right) \left(\frac{\epsilon_{\rm SN}}{0.05}\right)$$
$$\times \left(\frac{E_{\rm SN}}{10^{51} {\rm erg}}\right) \left(\frac{M_{\rm vir}}{10^{12} M_\odot}\right)^{-2/3} \left(\frac{1+z}{4}\right)^{-1}. \tag{A6}$$

We adopt the following values: number of SNe per unit solar mass of condensed stars $N_{\rm SN} \simeq 1.4 \times 10^{-2}/M_\odot$; fraction of the released energy used to heat the gas $\epsilon_{\rm SN} = 0.05$; kinetic energy released per SN $E_{\rm SN} \simeq 10^{51}$ erg; halo binding energy

$E_{\rm bind} \simeq 3.2 \times 10^{14} (M_{\rm vir}/10^{12} M_\odot)^{2/3} ([(1 + z)/4]$ cm^2 s^{-2} (Mo & Mao 2004).

The infrared luminosity (8–1000 μm) associated with dust enshrouded star formation is

$$L_{\star,{\rm IR}}(t) = k_{\star,{\rm IR}} \times 10^{43} \left(\frac{\dot{M}_\star}{M_\odot \ {\rm yr}^{-1}}\right) {\rm erg \ s}^{-1}, \tag{A7}$$

where the coefficient $k_{\star,{\rm IR}}$ depends on the SED. We adopt $k_{\star,{\rm IR}} \sim 3$ (Lapi et al. 2011; Kennicutt 1998).

The cold gas inflow rate into the reservoir around the supermassive black hole, driven by radiation drag, is given by

$$\dot{M}_{\rm inflow} \simeq \frac{L_\star}{c^2}(1 - e^{-\tau_{\rm RD}}) \simeq \alpha_{\rm RD} \times 10^{-3} \dot{M}_\star (1 - e^{-\tau_{\rm RD}}), \tag{A8}$$

with

$$\tau_{\rm RD}(t) = \tau_{\rm RD}^0 \left(\frac{Z_{\rm cold}(t)}{Z_\odot}\right) \left(\frac{M_{\rm cold}}{10^{12} M_\odot}\right) \left(\frac{M_{\rm vir}}{10^{13} M_\odot}\right)^{-2/3}. \tag{A9}$$

For the strength of the radiation drag, we adopt $\alpha_{\rm RD} = 2.5$ and set $\tau_{\rm RD}^0 = 3.0$. The model also follows the evolution of the cold gas metallicity, $Z_{\rm cold}(t)$. An approximate solution of the equations governing the chemical evolution is (A. Lapi et al., in preparation)

$$Z_{\rm cold}(t) = Z_{\rm inf}^0 + \frac{s}{s\gamma - 1}\mathcal{E}_Z(t) - \frac{st/t_{\rm cond}}{e^{(s\gamma-1)t/t_{\rm cond}} - 1}$$
$$\cdot \left\{\mathcal{E}_Z(t) + B_Z \sum_{i=2}^{\infty} \frac{1}{i \cdot i!} \left[(s\gamma - 1)\frac{\min(t, t_Z)}{t_{\rm cond}}\right]^{i-1}\right\}, \tag{A10}$$

where $\gamma = 1 - \mathcal{R} - \beta_{\rm SN}$, the metallicity of the primordial infalling gas is $Z_{\rm inf}^0 = 10^{-5}$, and the mass fraction of newly formed metals ejected from stars, $\mathcal{E}_Z(t)$ is given by

$$\simeq A_Z + B_Z \ln\left[\frac{\min(t, t_{\rm saturation})}{t_Z}\right], \tag{A11}$$

with $A_Z = 0.03$, $B_Z = 0.02$, $t_Z = 20$ Myr, and $t_{\rm saturation} = 40$ Myr for the Chabrier's IMF ($Z_\odot \simeq 0.02$). Equation (A11) accounts for the fact that, soon after the onset of star formation, the metal yield, mainly contributed by stars with large masses ($\geqslant 20 M_\odot$) and short lifetimes ($t_Z \leqslant 20$ Myr), is a relatively large fraction of the initial stellar mass ($f_{\rm metal} \geqslant 0.12$) while, as the star formation proceeds, it progressively lowers to $f_{\rm metal} \sim 0.06$ as the main contribution shifts to stars with intermediate masses ~ 9–$20 M_\odot$ and lifetimes $t_Z \sim 20$–40 Myr, and finally saturates to values $f_{\rm metal} \sim 0.013$ as stars with masses $\leqslant 9 M_\odot$ and long lifetimes ($t_{\rm saturation} \geqslant 40$ Myr) take over (Bressan et al. 1998). The two parameters A_Z and B_Z depends mainly on the IMF.

The accretion rate into the central black hole obeys the equation

$$\dot{M}_{\rm BH} = \min\left(\dot{M}_{\rm BH}^{\rm visc}, \lambda_{\rm Edd} \dot{M}_{\rm Edd}\right), \tag{A12}$$

where $\dot{M}_{\rm BH}^{\rm visc}$ is the accretion rate allowed by the viscous dissipation of the angular momentum of the gas in the reservoir

$$\dot{M}_{\rm BH}^{\rm visc} = \frac{M_{\rm res}}{\tau_{\rm visc}} = \kappa_{\rm accr} \ 5 \times 10^3 \left(\frac{V_{\rm vir}}{500 \ {\rm km \ s}^{-1}}\right)^3$$
$$\times \left(\frac{M_{\rm res}}{M_\bullet}\right)^{3/2} \left(1 + \frac{M_\bullet}{M_{\rm res}}\right)^{1/2}, \tag{A13}$$
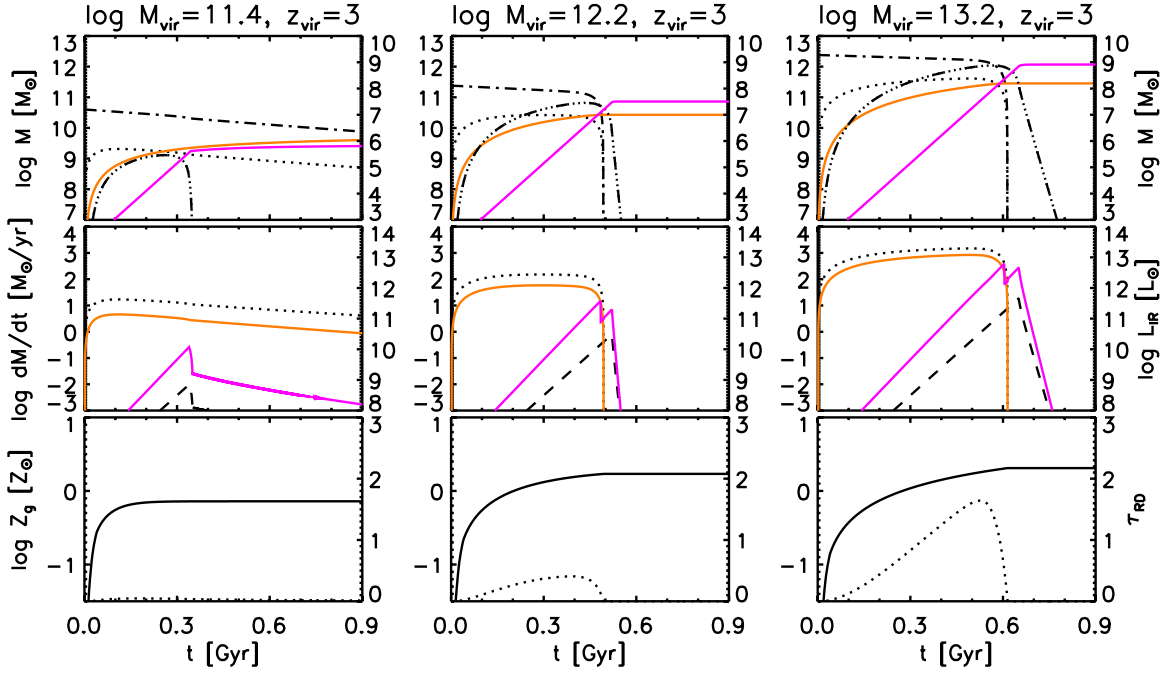
Figure 18. Evolution with galactic age of properties of the stellar and of the AGN component of proto-spheroidal galaxies virialized at $z_{vir} = 3$ for three choices of the virial (mostly dark matter) mass: $\log(M_{vir}/M_\odot) = 11.4$ (left-hand column), 12.4 (central column), and 13.2 (right-hand column). In the first row, the left y-axis scale refers to masses related to the stellar component (infalling hot gas mass (dot-dashed line), cold gas mass (dotted line), stellar mass ($M_\star$, solid orange line)), while the right-hand scale refers to quantities related to the AGN component (reservoir mass (triple-dot-dashed line) and black hole mass ($M_\bullet$, solid magenta line)). In the second row the left-hand scale refers to the SFR (dotted line) and to the BH accretion rate (dashed black line), while the right-hand scale refer to the IR (8–1000 μm) luminosity of the stellar (solid orange line) and of the AGN (solid magenta line) component. In the third row the left-hand scale refers to the gas metallicity (solid line), while the right-hand scale refers to the optical depth of individual gas clouds (dotted line).

(A color version of this figure is available in the online journal.)

with $\kappa_{accr} \simeq 10^{-2}$ and $V_{vir}^2 = GM_{vir}^{2/3}[4\pi\Delta_{vir}(z)\bar\rho_m(z)/3]^{1/3}$, Δ_{vir} being the overdensity of a virialized halo at redshift z_{vir} within its virial radius r_{vir}. $\dot{M}_{Edd} \equiv M_\bullet/\epsilon\, t_{Edd}$ is the accretion rate corresponding to the Eddington luminosity given the mass-to-light conversion efficiency ϵ (we set $\epsilon = 0.1$ so that the Salpeter time $\epsilon\, t_{Edd} = 4.5 \times 10^7$ yr) and $\lambda_{Edd}(z)$ is the Eddington ratio that we assume to slightly increase with redshift for $z \gtrsim 1.5$

$$\lambda_{Edd}(z) \simeq 0.1(z - 1.5)^2 + 1.0 \qquad (A14)$$

up to a maximum value $\lambda_{Edd,max} = 4$. The growth rate of the black hole mass is

$$\dot{M}_\bullet(t) = (1 - \epsilon)\dot{M}_{BH} \qquad (A15)$$

starting from a seed mass $M_\bullet^{seed} = 10^2\, M_\odot$. The bolometric AGN luminosity is

$$L_\bullet = \epsilon\dot{M}_{BH}c^2 = 5.67 \times 10^{45}\left(\frac{\epsilon}{0.1}\right)\left(\frac{\dot{M}_{BH}}{M_\odot\, yr^{-1}}\right) \text{ erg s}^{-1}. \qquad (A16)$$

A minor fraction of it couples with the ISM of the host galaxy giving rise to an outflow at a rate

$$\dot{M}_{inf,cold}^{QSO} = \dot{M}_{wind}\frac{M_{inf,cold}}{M_{inf} + M_{cold}}, \qquad (A17)$$

with

$$\dot{M}_{wind} = \frac{L_{QSO}^{ISM}}{E_{bind}}, \qquad (A18)$$

and

$$L_{QSO}^{ISM} \simeq 2 \times 10^{44}\epsilon_{QSO}\left(\frac{\dot{M}_{BH}}{M_\odot\, yr^{-1}}\right)^{3/2} \text{ erg s}^{-1}. \qquad (A19)$$

L_{QSO}^{ISM} is the mechanical AGN luminosity, used to unbind the gas. The coefficient quantifying the strength of the QSO feedback is chosen to be $\epsilon_{QSO} = 3$. The ratio of the mechanical to the total AGN luminosity

$$L_{QSO}^{ISM}/L_\bullet \simeq 3.5 \times 10^{-3}\frac{\epsilon_{QSO}}{\epsilon}\left(\frac{\dot{M}_{BH}}{M_\odot\, yr^{-1}}\right)^{1/2}, \qquad (A20)$$

is constrained to be in the range 0.006–0.15.

Examples of the resulting evolution with galactic age of properties of the stellar and of the AGN component are shown in Figure 18 for three values of the virial mass and $z_{vir} = 3$.

As mentioned in Section 5, to improve the fits of the data we have modified, by trial and error, the values of some model parameters used in previous papers, still within their plausible ranges (see Table 2). The impact of these parameters on the derived LFs can be more easily understood with reference to the time lag between the halo virialization and the peak in black hole accretion rate, Δt_{peak} (Lapi et al. 2006). The duration of star formation is $\Delta t_{SF} \lesssim \Delta t_{peak}$ (see Figure 18) due to the drastic effect of QSO feedback in massive halos which dominate the bright end of the LFs. Note that longer Δt_{peak} (or Δt_{SF}) imply higher bright tails of the LFs. The final black hole mass increases with increasing the coefficient, τ_{RD}^0, of the optical depth of gas clouds (Equation (A9)) because it implies a higher efficiency of the radiation drag driving the gas into the reservoir.

There is a degeneracy, to some extent, between τ_{RD}^0 and the gas metallicity Z_{cold}, implying that τ_{RD}^0 cannot be tightly constrained (see Granato et al. 2004). The value of Δt_{peak} grows substantially in response to a small increase of the radiative efficiency ϵ that yields a slower growth of the black hole mass and a weaker QSO feedback. Higher values of the Eddington ratio, λ_{Edd}, result in lower values of both Δt_{peak} and of the final black hole mass. A rise of λ_{Edd} at high-z is required to account for the observed space density of very luminous QSOs (see the high-z data in Figure 7 and Figure 8; Lapi et al. 2006). A higher QSO feedback efficiency (higher ϵ_{QSO}) shortens the duration of star formation, Δt_{SF}, but has a minor effect on Δt_{peak} and on the final black hole mass. Finally, the coefficient relating the SFR to the IR luminosity, $k_{\star,IR}$, varies with age mix of stellar populations, chemical composition, and IMF. Increasing it, we shift the LFs toward higher luminosities.

REFERENCES

Altieri, B., Berta, S., Lutz, D., et al. 2010, A&A, 518, L17
Angulo, R. E., Springel, V., White, S. D. M., et al. 2012, MNRAS, 426, 2046
Aretxaga, I., Hughes, D. H., Coppin, K., et al. 2007, MNRAS, 379, 1571
Aretxaga, I., Wilson, G. W., Aguilar, E., et al. 2011, MNRAS, 415, 3831
Assef, R. J., Kochanek, C. S., Ashby, M. L. N., et al. 2011, ApJ, 728, 56
Austermann, J. E., Aretxaga, I., Hughes, D. H., et al. 2009, MNRAS, 393, 1573
Austermann, J. E., Dunlop, J. S., Perera, T. A., et al. 2010, MNRAS, 401, 160
Ballantyne, D. R., & Papovich, C. 2007, ApJ, 660, 988
Bardeen, J. M., Bond, J. R., Kaiser, N., & Szalay, A. S. 1986, ApJ, 304, 15
Baugh, C. M., Lacey, C. G., Frenk, C. S., et al. 2005, MNRAS, 356, 1191
Bernardi, M., Shankar, F., Hyde, J. B., et al. 2010, MNRAS, 404, 2087
Berta, S., Magnelli, B., Nordon, R., et al. 2011, A&A, 532, A49
Béthermin, M., Daddi, E., Magdis, G., et al. 2012a, ApJL, 757, L23
Béthermin, M., Dole, H., Beelen, A., & Aussel, H. 2010, A&A, 512, A78
Béthermin, M., Dole, H., Lagache, G., Le Borgne, D., & Penin, A. 2011, A&A, 529, A4
Béthermin, M., Le Floc'h, E., Ilbert, O., et al. 2012b, A&A, 542, A58
Blain, A. W. 1996, MNRAS, 283, 1340
Boylan-Kolchin, M., Springel, V., White, S. D. M., Jenkins, A., & Lemson, G. 2009, MNRAS, 398, 1150
Bressan, A., Granato, G. L., & Silva, L. 1998, A&A, 332, 135
Brown, M. J. I., Brand, K., Dey, A., et al. 2006, ApJ, 638, 88
Burgarella, D., Buat, V., Takeuchi, T. T., Wada, T., & Pearson, C. 2009, PASJ, 61, 177
Burlon, D., Ajello, M., Greiner, J., et al. 2011, ApJ, 728, 58
Caputi, K. I., Lagache, G., Yan, L., et al. 2007, ApJ, 660, 97
Carroll, S. M., Press, W. H., & Turner, E. L. 1992, ARA&A, 30, 499
Chabrier, G. 2003, PASP, 115, 763
Chapman, S. C., Blain, A. W., Smail, I., & Ivison, R. J. 2005, ApJ, 622, 772
Chapman, S. C., Helou, G., Lewis, G. F., & Dale, D. A. 2003, ApJ, 588, 186
Chen, C.-C., Cowie, L. L., Wang, W.-H., Barger, A. J., & Williams, J. P. 2011, ApJ, 733, 64
Cirasuolo, M., Shankar, F., Granato, G. L., De Zotti, G., & Danese, L. 2005, ApJ, 629, 816
Clements, D. L., Bendo, G., Pearson, C., et al. 2011, MNRAS, 411, 373
Clements, D. L., Rigby, E., Maddox, S., et al. 2010, A&A, 518, L8
Colavitti, E., Matteucci, F., & Murante, G. 2008, A&A, 483, 401
Cook, M., Lapi, A., & Granato, G. L. 2009, MNRAS, 397, 534
Coppin, K., Chapin, E. L., Mortier, A. M. J., et al. 2006, MNRAS, 372, 1621
Croom, S. M., Richards, G. T., Shanks, T., et al. 2009, MNRAS, 399, 1755
Croom, S. M., Smith, R. J., Boyle, B. J., et al. 2004, MNRAS, 349, 1397
da Cunha, E., Charlot, S., Dunne, L., Smith, D., & Rowlands, K. 2012, in IAU Symp. 284, The Spectral Energy Distribution of Galaxies, ed. R. J. Tuffs & C. C. Popescu (Cambridge: Cambridge Univ. Press), 292
Dale, D. A., & Helou, G. 2002, ApJ, 576, 159
Dole, H., Lagache, G., Puget, J.-L., et al. 2006, A&A, 451, 417
Dole, H., Le Floc'h, E., Pérez-González, P. G., et al. 2004, ApJS, 154, 87
Dufresne, D. 2004, Adv. Appl. Probab., 36, 747
Dunne, L., Eales, S., Edmunds, M., et al. 2000, MNRAS, 315, 115
Eales, S. A., Raymond, G., Roseboom, I. G., et al. 2010, A&A, 518, L23
Elbaz, D., Cesarsky, C. J., Chanial, P., et al. 2002, A&A, 384, 848
Elbaz, D., Cesarsky, C. J., Fadda, D., et al. 1999, A&A, 351, L37
Fan, L., Lapi, A., Bressan, A., et al. 2010, ApJ, 718, 1460

Fontanot, F., Somerville, R. S., Silva, L., Monaco, P., & Skibba, R. 2009, MNRAS, 392, 553
Franceschini, A., Rodighiero, G., Vaccari, M., et al. 2010, A&A, 517, A74
Frayer, D. T., Fadda, D., Yan, L., et al. 2006, AJ, 131, 250
Fu, H., Yan, L., Scoville, N. Z., et al. 2010, ApJ, 722, 653
Fukugita, M., Ichikawa, T., Gunn, J. E., et al. 1996, AJ, 111, 1748
Glenn, J., Conley, A., Béthermin, M., et al. 2010, MNRAS, 409, 109
González-Nuevo, J., Lapi, A., Fleuren, S., et al. 2012, ApJ, 749, 65
Granato, G. L., & Danese, L. 1994, MNRAS, 268, 235
Granato, G. L., De Zotti, G., Silva, L., Bressan, A., & Danese, L. 2004, ApJ, 600, 580
Greve, T. R., Vieira, J. D., Weiß, A., et al. 2012, ApJ, 756, 101
Greve, T. R., Weiß, A., Walter, F., et al. 2010, ApJ, 719, 483
Gruppioni, C., Lari, C., Pozzi, F., et al. 2002, MNRAS, 335, 831
Gruppioni, C., Pozzi, F., Andreani, P., et al. 2010, A&A, 518, L27
Gruppioni, C., Pozzi, F., Zamorani, G., & Vignali, C. 2011, MNRAS, 416, 70
Hartwick, F. D. A., & Schade, D. 1990, ARA&A, 28, 437
Hatsukade, B., Kohno, K., Aretxaga, I., et al. 2011, MNRAS, 411, 102
Hayward, C. C., Narayanan, D., Kereš, D., et al. 2013, MNRAS, 428, 2529
Hopwood, R., Serjeant, S., Negrello, M., et al. 2010, ApJL, 716, L45
Ivison, R. J., Swinbank, A. M., Swinyard, B., et al. 2010, A&A, 518, L35
Jain, B., & Lima, M. 2011, MNRAS, 411, 2113
Johansson, D., Sigurdarson, H., & Horellou, C. 2011, A&A, 527, A117
Kaviani, A., Haehnelt, M. G., & Kauffmann, G. 2003, MNRAS, 340, 739
Kennicutt, R. C., Jr. 1998, ARA&A, 36, 189
Kim, H.-S., Lacey, C. G., Cole, S., et al. 2012, MNRAS, 425, 2674
Klypin, A. A., Trujillo-Gomez, S., & Primack, J. 2011, ApJ, 740, 102
Knudsen, K. K., van der Werf, P. P., & Kneib, J.-P. 2008, MNRAS, 384, 1611
Lacey, C. G., Baugh, C. M., Frenk, C. S., et al. 2008, MNRAS, 385, 1155
Lacey, C. G., Baugh, C. M., Frenk, C. S., et al. 2010, MNRAS, 405, 2
Lagache, G., Abergel, A., Boulanger, F., Désert, F. X., & Puget, J.-L. 1999, A&A, 344, 322
Lahav, O., Lilje, P. B., Primack, J. R., & Rees, M. J. 1991, MNRAS, 251, 128
Lapi, A., & Cavaliere, A. 2011, ApJ, 743, 127
Lapi, A., González-Nuevo, J., Fan, L., et al. 2011, ApJ, 742, 24
Lapi, A., Negrello, M., González-Nuevo, J., et al. 2012, ApJ, 755, 46
Lapi, A., Shankar, F., Mao, J., et al. 2006, ApJ, 650, 42
Lawrence, A. 1991, MNRAS, 252, 586
Le Borgne, D., Elbaz, D., Ocvirk, P., & Pichon, C. 2009, A&A, 504, 727
Le Floc'h, E., Aussel, H., Ilbert, O., et al. 2009, ApJ, 703, 222
Le Floc'h, E., Papovich, C., Dole, H., et al. 2005, ApJ, 632, 169
Magnelli, B., Elbaz, D., Chary, R. R., et al. 2009, A&A, 496, 57
Magnelli, B., Elbaz, D., Chary, R. R., et al. 2011, A&A, 528, A35
Mao, J., Lapi, A., Granato, G. L., de Zotti, G., & Danese, L. 2007, ApJ, 667, 655
Markwardt, C. B. 2009, in ASP Conf. Ser. 411, Astronomical Data Analysis Software and Systems XVIII, ed. D. A. Bohlender, D. Durand, & P. Dowler (San Francisco, CA: ASP), 251
Marsden, G., Ade, P. A. R., Bock, J. J., et al. 2009, ApJ, 707, 1729
Marsden, G., Chapin, E. L., Halpern, M., et al. 2011, MNRAS, 417, 1192
Matute, I., La Franca, F., Pozzi, F., et al. 2006, A&A, 451, 443
Mazzei, P., Della Valle, A., & Bettoni, D. 2007, A&A, 462, 21
Mazzei, P., Xu, C., & de Zotti, G. 1992, A&A, 256, 45
Miville-Deschênes, M.-A., Lagache, G., & Puget, J.-L. 2002, A&A, 393, 749
Mo, H. J., & Mao, S. 2004, MNRAS, 353, 829
Moré, J. 1978, in Numerical Analysis, Vol. 630, ed. G. A. Watson (Berlin: Springer), 105
Nakamura, T. T., & Suto, Y. 1997, PThPh, 97, 49
Narayanan, D., Hayward, C. C., Cox, T. J., et al. 2010, MNRAS, 401, 1613
Negrello, M., Clemens, M., Gonzalez-Nuevo, J., et al. 2013, MNRAS, 429, 1309
Negrello, M., Hopwood, R., De Zotti, G., et al. 2010, Sci, 330, 800
Negrello, M., Perrotta, F., González-Nuevo, J., et al. 2007, MNRAS, 377, 1557
Niemi, S.-M., Somerville, R. S., Ferguson, H. C., et al. 2012, MNRAS, 421, 1539
Noble, A. G., Webb, T. M. A., Ellingson, E., et al. 2012, MNRAS, 419, 1983
Oliver, S. J., Wang, L., Smith, A. J., et al. 2010, A&A, 518, L21
Palanque-Delabrouille, N., Magneville, Ch., Yeche, Ch., et al. 2013, A&A, 551, A29
Papovich, C., Dole, H., Egami, E., et al. 2004, ApJS, 154, 70
Patanchon, G., Ade, P. A. R., Bock, J. J., et al. 2009, ApJ, 707, 1750
Pearson, C. P., Oyabu, S., Wada, T., et al. 2010, A&A, 514, A8
Pei, Y. C. 1995, ApJ, 438, 623
Pénin, A., Lagache, G., Noriega-Crespo, A., et al. 2012, A&A, 543, A123
Perrotta, F., Baccigalupi, C., Bartelmann, M., De Zotti, G., & Granato, G. L. 2002, MNRAS, 329, 445
Perrotta, F., Magliocchetti, M., Baccigalupi, C., et al. 2003, MNRAS, 338, 623

Planck Collaboration. 2013, A&A, 550, A133
Polletta, M., Tajer, M., Maraschi, L., et al. 2007, ApJ, 663, 81
Pozzi, F., Gruppioni, C., Oliver, S., et al. 2004, ApJ, 609, 122
Rahmati, A., & van der Werf, P. P. 2011, MNRAS, 418, 176
Reddy, N., Dickinson, M., Elbaz, D., et al. 2012, ApJ, 744, 154
Renault, C., Barrau, A., Lagache, G., & Puget, J.-L. 2001, A&A, 371, 771
Renzini, A. 2006, ARA&A, 44, 141
Richards, G. T., Lacy, M., Storrie-Lombardi, L. J., et al. 2006, ApJS, 166, 470
Rieke, G. H., Blaylock, M., Decin, L., et al. 2008, AJ, 135, 2245
Rodighiero, G., Vaccari, M., Franceschini, A., et al. 2010, A&A, 515, A8
Ross, N. P., McGreer, I. D., White, M., et al. 2012, arXiv:1210.6389
Rowan-Robinson, M. 2009, MNRAS, 394, 117
Saunders, W., Rowan-Robinson, M., Lawrence, A., et al. 1990, MNRAS, 242, 318
Scott, K. S., Wilson, G. W., Aretxaga, I., et al. 2012, MNRAS, 423, 575
Scott, K. S., Yun, M. S., Wilson, G. W., et al. 2010, MNRAS, 405, 2260
Sedgwick, C., Serjeant, S., Pearson, C., et al. 2011, MNRAS, 416, 1862
Shankar, F., Lapi, A., Salucci, P., De Zotti, G., & Danese, L. 2006, ApJ, 643, 14
Sheth, R. K., & Tormen, G. 1999, MNRAS, 308, 119
Shimizu, I., Yoshida, N., & Okamoto, T. 2012, MNRAS, 427, 2866
Shupe, D. L., Rowan-Robinson, M., Lonsdale, C. J., et al. 2008, AJ, 135, 1050
Silva, L., Granato, G. L., Bressan, A., & Danese, L. 1998, ApJ, 509, 103
Smail, I., Ivison, R. J., Blain, A. W., & Kneib, J.-P. 2002, MNRAS, 331, 495
Smith, D. J. B., Dunne, L., da Cunha, E., et al. 2012, MNRAS, 427, 703
Smolčić, V., Aravena, M., Navarrete, F., et al. 2012, A&A, 548, 4
Soifer, B. T., & Neugebauer, G. 1991, AJ, 101, 354
Spinoglio, L., & Malkan, M. A. 1989, ApJ, 342, 83
Springel, V., White, S. D. M., Jenkins, A., et al. 2005, Natur, 435, 629
Stecker, F. W., & de Jager, O. C. 1997, ApJ, 476, 712
Sugiyama, N. 1995, ApJS, 100, 281
Swinbank, A. M., Smail, I., Longmore, S., et al. 2010, Natur, 464, 733
Tacconi, L. J., Genzel, R., Smail, I., et al. 2008, ApJ, 680, 246
Takagi, T., Matsuhara, H., Goto, T., et al. 2012, A&A, 537, A24
Takeuchi, T. T., Yoshikawa, K., & Ishii, T. T. 2003, ApJL, 587, L89
Teplitz, H. I., Chary, R., Elbaz, D., et al. 2011, AJ, 141, 1
Treister, E., Urry, C. M., Van Duyne, J., et al. 2006, ApJ, 640, 603
Vaccari, M., Marchetti, L., Franceschini, A., et al. 2010, A&A, 518, L20
Valiante, E., Lutz, D., Sturm, E., Genzel, R., & Chapin, E. L. 2009, ApJ, 701, 1814
Vieira, J. D., Crawford, T. M., Switzer, E. R., et al. 2010, ApJ, 719, 763
Viero, M. P., Wang, L., Zemcov, M., et al. 2012, arXiv:1208.5049
Wada, T., Oyabu, S., Ita, Y., et al. 2007, PASJ, 59, 515
Wang, J., Navarro, J. F., Frenk, C. S., et al. 2011, MNRAS, 413, 1373
Warren, S. J., Hewett, P. C., & Osmer, P. S. 1994, ApJ, 421, 412
Wu, Y., Shi, Y., Helou, G., et al. 2011, ApJ, 734, 40
Xia, J.-Q., Negrello, M., Lapi, A., et al. 2012, MNRAS, 422, 1324
Yun, M. S., Scott, K. S., Guo, Y., et al. 2012, MNRAS, 420, 957
Zemcov, M., Blain, A., Halpern, M., & Levenson, L. 2010, ApJ, 721, 424
Zhao, D. H., Mo, H. J., Jing, Y. P., & Börner, G. 2003, MNRAS, 339, 12
Zheng, Z., Berlind, A. A., Weinberg, D. H., et al. 2005, ApJ, 633, 791